

1
2
3
4
5
6
7
8
9
10
11
12
13
14
15
16
17
18
19
20
21
22
23
24
25
26

**A Simple Model for Tropical Convective Cloud Shield Area Growth and Decay Rates
Informed by Geostationary IR, GPM, and Aqua/AIRS Satellite Data**

Gregory S. Elsaesser^{1,2}, Rémy Roca³, Thomas Fiolleau³,

Anthony D. Del Genio^{2,†}, Jingbo Wu^{1,2}

¹*Department of Applied Physics and Mathematics, Columbia University, New York, New York, USA*

²*NASA Goddard Institute for Space Studies, 2880 Broadway, New York, New York, USA*

³*Laboratoire d'Etudes en Géophysique et Océanographie Spatiales, Observatoire Midi-Pyrénées, Toulouse, France*

Corresponding Author: Gregory S. Elsaesser, Department of Applied Physics and Applied Mathematics, Columbia University/NASA Goddard Institute for Space Studies, 2880 Broadway, New York, New York, Tel: (212) 678-5596, gregory.elsaesser@columbia.edu

[†]*Now retired*

Key Points:

- A simple analytical model for cloud area growth and decay rates is developed, with a source term driven by convective cell diabatic heating.
- The model works equally well for convective systems of varying duration and degrees of convective organization over both land and ocean.
- The model suggests that a convective area fraction of ~ 0.2 is needed for stratiform cloud area maintenance.

27 **Abstract**

28 Deep convective system maximum areal extent is driven by the stratiform anvil area since
29 convective area fractions are much less than unity when systems reach peak size. It is important
30 to understand the processes that drive system size given the impact large systems have on rainfall
31 and that of anvils on high cloud feedbacks. Using satellite diabatic heating and convective-
32 stratiform information mapped to convective systems, composite analyses suggest that system
33 maximum sizes occur at the temporal mid-point of system lifecycles with both maximum size and
34 duration correlating with peak heating above the melting level. However, variations in system
35 growth rates exist, with the overall smooth composites emerging as the average of highly variable
36 system trajectories. Thus, this study focuses on understanding convective system growth rates on
37 short (30-minute) timescales via development of a simple analytical source – sink model that
38 predicts system area changes. Growth occurs when detrained convective mass (inferred from the
39 vertical gradient of diabatic heating and temperature lapse rates) and/or generation of convective
40 area exceeds a sink term whose magnitude is proportional to the current cloud shield size. The
41 model works well for systems over land and ocean, and for systems characterized by varying
42 degrees of convective organization and duration (1.5–35 hr, with correlations often >0.8 across
43 lifetime bins). The model may serve as a useful foundation for improved understanding of
44 processes driving changes in tropics-wide convective system cloud shields, and further supports
45 conceptual development and evaluation of prognostic climate model stratiform anvil area
46 parameterizations.

47 **1 Introduction**

48 Mesoscale convective systems (MCSs) are the dominant sources of rainfall in the tropics
49 (Tao and Moncrieff, 2009; Roca et al., 2014; Moncrieff, 2019). MCS cloud shields comprise
50 convective regions whose spatial aggregation may be quantified via “organization metrics” (Parker
51 and Johnson, 2000; Tobin et al., 2012; Tobin et al., 2013; Holloway et al., 2017; Retsch et al., 2020)
52 such that increased organization may be associated with larger cloud shields, longer lifetimes and
53 substantial rainfall accumulation (Liu et al., 2008; Liu, 2011; Roca and Fiolleau, 2020; Schiro et al.,
54 2020). High resolution model simulations over domains populated by MCSs are frequent sources
55 for deriving MCS radiation, cloud, and rainfall lifecycle evolutions (Hagos et al., 2013; Feng et al.,
56 2018; Feng et al., 2021). Observational composite MCS evolutions can be derived by mapping
57 orbital-level satellite-estimated radiation, cloud, rainfall, and environment characteristics to the life
58 stages of IR-tracked MCSs (as in Machado et al., 1998; Machado and Laurent, 2004; Futyan and
59 Del Genio, 2007; Feng et al., 2012; Fiolleau and Roca, 2013b; Bouniol et al., 2016; Vant-Hull et al.,
60 2016; Roca et al., 2017; Roca et al., 2020), or by mapping in situ environmental data to scanning
61 radar-identified MCSs (e.g., Wang et al., 2019; Wang et al., 2020). One such compositing analysis
62 has revealed that MCSs over the open ocean cool the sea surface temperature (SST), a signature that
63 lasts for days (Duncan et al., 2014) and is likely to affect the subsequent development of convection.

64 MCS convective regions are characterized by diabatic heating profiles whose magnitudes are
65 positive throughout most of the troposphere, though spread over a smaller area, while the extensive
66 moderately raining stratiform anvil region is characterized by widespread positive heating that peaks
67 above the melting level with diabatic cooling below (Elsaesser et al., 2010; Liu et al., 2015; Feng et
68 al., 2018) attributed to melting snow and precipitation evaporation below cloud base. The heating
69 profiles combine to yield top-heavy system-average heating profiles (Houze, 1989; Houze, 2004;
70 Elsaesser et al., 2010; Hannah et al., 2016; Feng et al., 2018) that tightly couple to large-scale tropical
71 circulations (Hartmann et al., 1984; Schumacher et al., 2004; Inoue and Back, 2015). Ice particles,
72 laterally detrained by convection, contribute to the growth of the raining stratiform anvil region.
73 Both the rate at which ice particles are detrained and particle fall speeds impact the areal extent of
74 the stratiform area. General circulation models (GCMs) are typically crude in their parameterization
75 of detrained ice (Elsaesser et al., 2017; Lin et al., 2021), and thus, have trouble simulating the growth
76 of stratiform area, let alone parameterizing MCSs (Moncrieff et al., 2017; Moncrieff, 2019).

77 However, GCMs may still simulate relatively unbiased global rainfall and diabatic heating
78 climatologies in the absence of successful MCS simulation, given that GCM tuning procedures focus
79 on improving mean states (Mauritsen et al., 2012; Schmidt et al., 2017) with little or no penalty for
80 discrepancies cancelling at the cloud-system scale. Structural parameterization errors are rarely
81 tuned away, and they manifest themselves in biased regional rainfall rate distributions, large-scale
82 modes of tropical variability, and cloud feedbacks. Accurate simulation of cloud feedbacks is
83 important, and since tropical high cloud fields are largely the product of convective detrainment
84 (Bony et al., 2016; Seeley et al., 2019) and residual MCS cloud shields, the contribution of tropical
85 high clouds to total cloud feedbacks may be quite related to how well MCSs are simulated in the
86 parent GCM. These complicated modes of convection are certainly one reason moist convection is
87 a large source of uncertainty in our ability to project climate change (e.g., Bony et al., 2015;
88 Schneider et al., 2017). Improved projections of regional rainfall distributions, more accurate
89 simulation of cloud feedbacks and equilibrium climate sensitivity, and improved understanding of
90 MCS trends emerging from high resolution simulations (Prein et al., 2017) and observations (Tan et
91 al., 2015) requires continued work on determining the dominant drivers of system evolutions and
92 their extensive cloud shields.

93 To this end, we perform new MCS observational analyses that build on previous MCS
94 lifecycle compositing studies (section 3.1) and then turn our attention to the often-variable MCS
95 cloud shield growth and decay rates, with a goal of understanding how these growth and decay rates
96 relate to diabatic heating profiles (section 3.2 and 3.3). Since the vertical derivative of diabatic
97 heating in convection ties to mass divergence, and mass divergence influences cloud shield changes,
98 we contribute to research aiming to determine the factors that drive changes in stratiform anvils (e.g.,
99 Seeley et al., 2019; Hagos et al., 2020) with a focus on the development of a simple analytical source-
100 sink model for cloud shield area changes informed by satellite data aggregated over the global tropics.
101 These analyses will serve as a conceptual framework for continued development of organized
102 convection parameterization in the GISS model, and can inform GCM convective parameterization
103 development more broadly.

104 **2 Data Sources**

105 *2.1 Satellite Observational Products*

106 Aqua AIRS/AMSU (Chahine et al., 2006) version 6 data for temperature (available for the
107 entire tropospheric column) and water vapor (for pressure levels > 300 hPa), along with Microwave
108 Limb Sounder (MLS; Waters et al., 2006) version 3 data for water vapor profiles at pressure levels
109 < 300 hPa, serve as the observed thermodynamic data sources in this work. Convective and
110 stratiform pixel identification (Level 2 data) derived from the Global Precipitation Measurement
111 (GPM; Skofronick-Jackson et al., 2017) mission Dual-frequency Precipitation Radar (DPR; Iguchi
112 et al., 2012) product, rainfall from the Level 2 combined (DPR+GMI; Grecu et al., 2016) product,
113 and diabatic heating (often denoted as Q_I-Q_R hereafter, or a heating term defined here that includes
114 all components except horizontal eddy flux convergence and radiative heating) from the Level 2
115 Convective-Stratiform Heating (CSH; Lang and Tao, 2018) and Spectral Latent Heating (SLH;
116 Shige et al., 2009) products serve as the observed convective and stratiform precipitation and heating
117 sources. AIRS/MLS and GPM orbital-level data are mapped to the MCS cloud shield provided by
118 the TOOCAN convective system tracking algorithm (Fiolleau and Roca, 2013a,b). For compositing
119 results shown in section 3, at least 1/3 of the system cloud shield must be sampled by GPM in order
120 for measurements to be included in averaging. In order for GPM overpass data to be used in the
121 analytical model development and associated coefficient estimation, at least 2/3 of the cloud shield
122 must be sampled by GPM. Sensitivity of some results to this coverage threshold is discussed in
123 section 3.4.

124 2.2 TOOCAN Convective System Tracking Database

125 The Tracking Of Organized Convection Algorithm through a 3-D segmentation (TOOCAN;
126 Fiolleau and Roca, 2013a) methodology, applied to infrared (IR) brightness temperature (BT) data
127 observed from a fleet of geostationary platforms, serve as our source of MCSs (defined here as
128 precipitating cloud systems, of spatial scale $O(100\text{km})$, that occur in connection with thunderstorms).
129 The TOOCAN approach aims to retain the spatial association between the convective region of
130 MCSs and their attendant stratiform anvil component. The algorithm operates within a space-time
131 volume of IR images, and applies a 3-D image processing technique to decompose the cold cloud
132 shield (delineated by a 235K threshold) in the spatio-temporal domain into component MCSs. The
133 algorithm is based on an iterative process of detection and dilation of convective seeds in the spatio-
134 temporal domain. Individual convective seeds are first detected in 3D by applying a given BT
135 threshold in the volume of IR images. Convective seeds with a minimum lifetime duration of 1.5h
136 and exceeding 625km^2 per frame are extracted. Each detected convective seed is spread in the spatio-

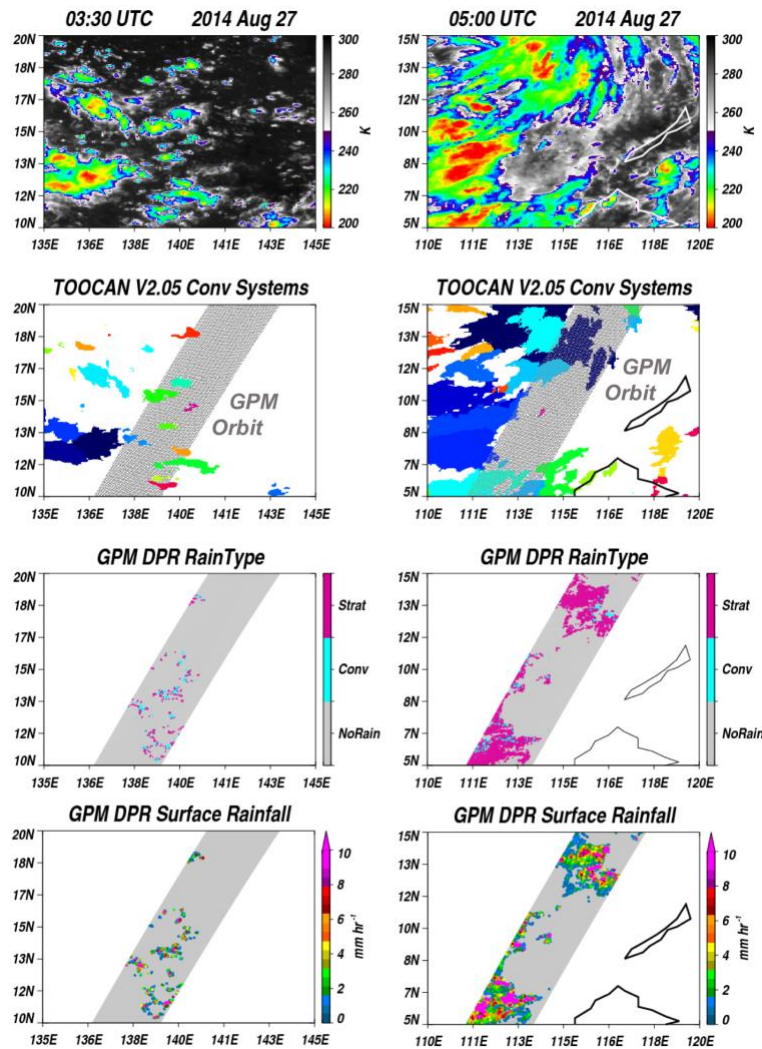
137 temporal domain until it reaches the intermediate cold cloud shield boundaries identified at a 5K
138 warmer BT threshold. This step consists in adding edge pixels belonging to the intermediate cold
139 cloud shield to all already detected seeds. The dilation of the convective seeds is performed by using
140 a 10-connected spatiotemporal neighborhood (8-connected spatial neighborhood and 2-connected
141 temporal neighborhood) to favor spatial dilation rather than the temporal dilation. Note that the pixel
142 aggregation process is constrained by a BT difference between the edge and current pixel, which has
143 to be greater than -1K to minimize the effects of local minima. The iterative process starts with a
144 detection of the convective seeds set at a 190K BT threshold, works with a 5K detection step, and is
145 stopped when the 235K threshold is reached. The TOOCAN algorithm is unique in that it avoids
146 the convective system split and merge artifacts associated with traditional tracking algorithms, thus
147 enabling MCSs and their attendant cloud shield sizes to be accurately tracked along their entire life
148 cycles from early initiation stages to the later dissipation stages.

149 For this study, IR from MSG-3, GOES-13 and 15, METEOSAT-7, and MTSAT-2 are used,
150 and MCSs within the tropical belt (30°S-30°N) from Mar – Dec 2014 are tracked. The IR sensors
151 hosted on geostationary platforms exhibit instrument and engineering differences (e.g., different
152 spatial and temporal resolutions, observation frequencies, spectral responses, calibrations). All IR
153 data have been remapped to a common 0.04° equal angle grid while the temporal resolution has been
154 unified to 30 minutes across all geostationary platforms to avoid an over-segmentation of the MCSs
155 detected (Fiolleau et al., 2020). Additionally, there has been an effort to inter-calibrate IR data across
156 sensors prior to ingestion into TOOCAN. The scanning schedule of MTSAT-2 does not provide a
157 half-hourly sampling of the Southern Hemisphere region at the time of this analysis; therefore, this
158 region is not considered in this study. Additionally, we only analyze convective systems if they are
159 separated from tropical cyclones, mid-latitude cyclones, and fronts. The IBTrACS database (Knapp
160 et al., 2010) and mid-latitude system databases (Naud et al., 2010; Naud et al., 2016) serve as the
161 sources for selecting which MCSs to remove, with roughly 40,000 GPM-intersected systems
162 remaining for analyses.

163 **3 Results**

164 3.1 Composite Convective System Diabatic Heating Lifecycles and System Durations

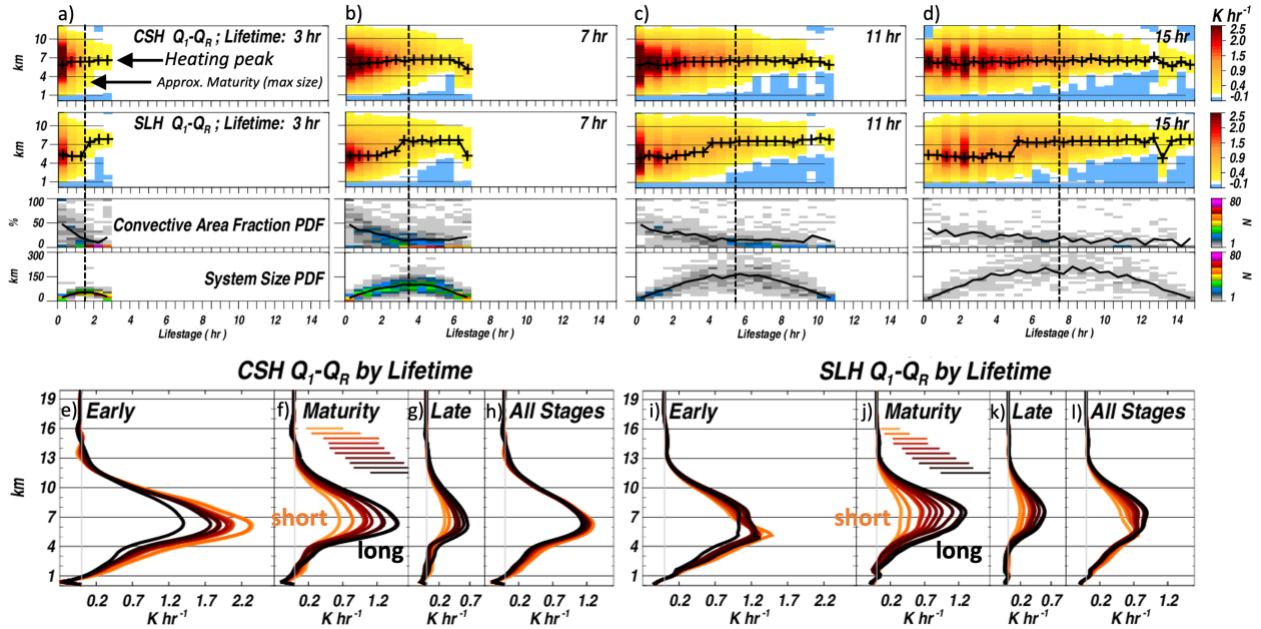
165 Several snapshots of convective systems are shown in Fig. 1. These examples suggest system
166 sizes are predominantly driven by changing stratiform areal extent, and to a much lesser extent,



167 **Figure 1.** (Left) From top to bottom, a snapshot (03:30 UTC, 2014 Aug 27) of IR brightness
 168 temperatures, observed convective systems (distinct systems are color-coded), GPM rain
 169 classification (stratiform, convective, no-surface-rain) , and GPM surface rainfall. (Right) as to
 170 the left, but for a different geographic location and time (05:00 UTC).

171
 172

173 varying convective extent. Close visual inspection of Fig. 1 shows that convective areas may be
 174 clustered on the edges of system shields or dispersed throughout, similar to Yuter and Houze (1998)
 175 and Fridlind et al. (2012), while anvil cloud shields extend beyond raining stratiform regions. For
 176 systems of varying durations, Fig. 2 shows the composite Q_I-Q_R , convective area fractions and
 177 system sizes as a function of system lifecycle stage. Most convective systems are irregularly shaped,
 178 and the “system size” computed (and often referred to hereafter) is the diameter of a circle whose
 179 area is equivalent to the TOOCAN-identified cloud shield area. At and shortly after initiation (i.e.,
 180 hr-0 life stage), convective area fractions and system sizes are similar regardless of system duration

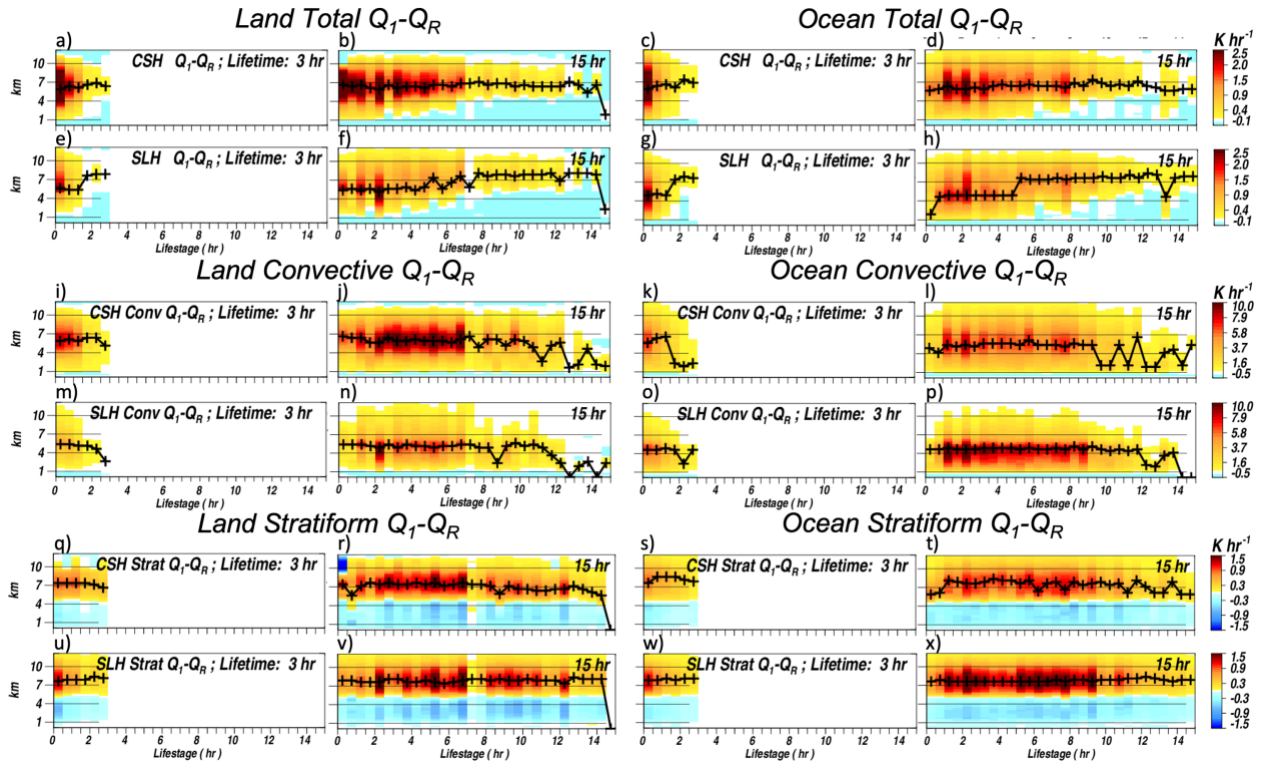


181
 182 **Figure 2.** (a – d) For convective systems of different durations (3-, 7-, 11- and 15-hr), the
 183 composite CSH and SLH Q_I-Q_R , convective area fractions, and system sizes (distributions are
 184 shown for the latter two variables to illustrate variability; solid lines denote average) as a function
 185 of system life stage. (e – l) The composite CSH and SLH Q_I-Q_R averaged over the early (initiation
 186 – 0.45), mature (0.45 – 0.55) and late (0.55 – termination) stages of the system lifecycles, color
 187 coded so that longer-lived systems are shaded darker (duration bins 3-, 5-, 7-, 9-, 11-, 13-, 15-, 19-
 188 , 25-, and 31-hr, respectively). For the mature-stage panels (f, j), horizontal lines denote the 1σ
 189 range in Q_I-Q_R at 7 km (also color coded by same duration bins).

190
 191 (Figs. 2a-d, third and fourth row), with SLH Q_I-Q_R being of comparable magnitude for all system
 192 durations (Fig. 2i), while CSH Q_I-Q_R is weaker in longer-lived vs shorter-lived systems (Fig. 2e).

193 The SLH product is developed using diabatic heating from Tropical Ocean Global
 194 Atmosphere-Coupled Ocean-Atmosphere Response Experiment (TOGA COARE) field campaign
 195 simulations while the CSH product is developed using 10 tropical land and ocean field campaign
 196 simulations, as discussed in Tao et al. (2016), so it is possible that similarity in SLH profiles during
 197 early stage convection (Fig. 2i) may reflect the use of Q_I-Q_R informed by one convection regime.
 198 TOGA COARE convection was also characterized by larger stratiform rainfall fractions (Tao et al.,
 199 2016) and further exhibited a very clear shallow – deep – stratiform transition (Lin et al., 2004;
 200 Kiladis et al. 2005). This may explain why, relative to CSH, the altitude of peak SLH Q_I-Q_R (Figs.
 201 2a-d, second rows) shifts upward as MCS life stages advance and why SLH Q_I-Q_R is more top heavy
 202 relative to CSH in overall composites (compare Figs. 2j-l to Figs. 2f-h).

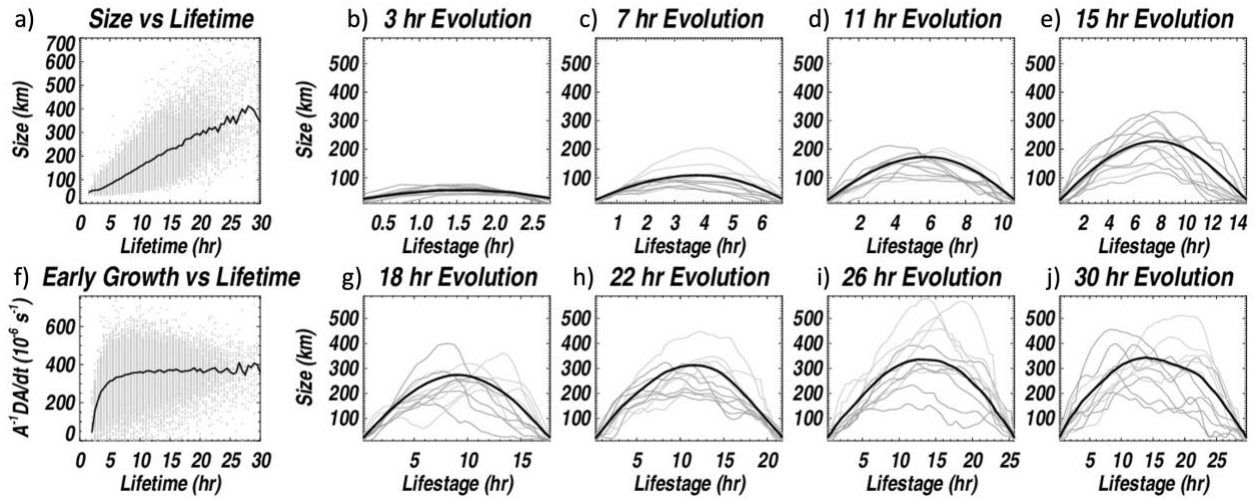
203 For the purposes of conveniently quantifying Q_I-Q_R at system peak, we define a “maturity”
 204 metric as the time at which a system reaches maximum size. At maturity, aside from longer-lived
 205 systems achieving a larger-size (evident from the system size PDFs), longer-lived systems are
 206 characterized by increased maximum Q_I-Q_R (typically near 7-km; Figs. 2f, j), with the 1σ range in
 207 peak heating for each system duration suggesting this is a robust result. Secondly, maturity marks
 208 the onset of near negligible Q_I-Q_R heating that begins in the boundary layer but gradually extends
 209 vertically to the melting level (~ 5 -km) as the system ages and dissipates (Figs. 2f-g, and Figs. 2j-k).
 210 Since convective area fractions reach their minimum near maturity and are nearly invariant thereafter
 211 (Figs. 2a-d, third rows), this implies that system vertical heating structures and convective-stratiform
 212 fractions do not uniquely map to each other. Furthermore, it is very clear that convective area
 213 fractions do not map uniquely to duration, either.



214
 215 **Figure 3.** For convective systems of 3 and 15-hr duration (over land and ocean separately), the
 216 CSH and SLH Q_I-Q_R as a function of system life stage (a – h). Composites are also partitioned into
 217 convective region-average (i – p) and stratiform region-average Q_I-Q_R (q – x) components. As in
 218 Fig. 2a-d, the plus symbols in each panel denote the altitude of peak heating as a function of life
 219 stage. Note the difference in Q_I-Q_R magnitude range and color scales across each panel, and
 220 relative to Fig. 2 ranges.

221 Fig. 3 shows Q_I-Q_R averaged over the convective and stratiform portions of the cloud shield
222 (in addition to system-average Q_I-Q_R composites in the top rows [Figs. 3a-g], as in Fig. 2). Fig. 3
223 suggests that CSH convective Q_I-Q_R is larger over land (Figs. 3i-j) than ocean (Figs. 3k-l), consistent
224 with studies documenting that convection over land is more intense (e.g., Zipser and Lemone, 1980;
225 Lucas et al., 1994; Takahashi et al., 2017; Takahashi et al., 2021). SLH shows the opposite behavior
226 in convective Q_I-Q_R (Figs. 3m-p), which again may be reflective of CSH retrievals being informed
227 by both land and ocean field campaigns, whereas SLH is informed solely by the TOGA COARE
228 oceanic convection environment. Both CSH and SLH yield similar stratiform heating composites
229 (Figs. 3q-x), perhaps a result of less innate variability in stratiform rain vertical structures (Houze,
230 1989; Schumacher and Houze, 2006) thus implying less dependence on CSH or SLH look-up tables
231 and algorithms. Since convective heating begins rapidly dissipating shortly before mid-lifecycle
232 stages (Figs. 3i-p), the weaker convective heating in the lower troposphere is eventually
233 overwhelmed by the nearly lifecycle-independent stratiform anvil cooling signature (Figs. 3q-x)
234 which results in system-average cooling below the melting level later in later life stages (Fig. 2 and
235 Figs. 3a-h). Despite the stratiform heating not varying substantially as a given system progresses, it
236 varies from one system duration to another, with longer-lived systems exhibiting slightly larger
237 amplitude stratiform heating-cooling signatures (Figs. 3q-x).

238 Are the composites shown in Figs. 2 and 3 representative of most convective systems?
239 Focusing on the middle lifecycle stages of convection systems, one interpretation of the system size
240 PDF variability (Figs. 2a-d, last row) is that systems hobble along, growing and decaying randomly,
241 with the time of maximum system size deviating from the temporal mid-point but with system
242 longevity mapping strongly to maximum size. Quantitatively, this would be reflected in a smaller
243 correlation between individual system size temporal evolutions and the composite system size
244 evolutions shown in Fig. 2. An alternate interpretation is that there is simply variability in the
245 maximum system size for a system of a given lifetime (with the maximum occurring at the temporal
246 mid-point), but with consistent increases in system size from initiation up to that point, and consistent
247 decay toward termination, thus implying high correlation between the composite evolution and
248 individual system evolutions. Fig. 4 sheds light on these questions. There is a clear relationship
249 between system size and lifetime (Fig. 4a; quantitatively, the percent variance explained between
250 maximum area and lifetime is $> 50\%$), similar to Feng et al. (2012) and shown in Roca et al. (2017).
251 There is, however, little relationship between growth at the early stages of convection and lifetime



252

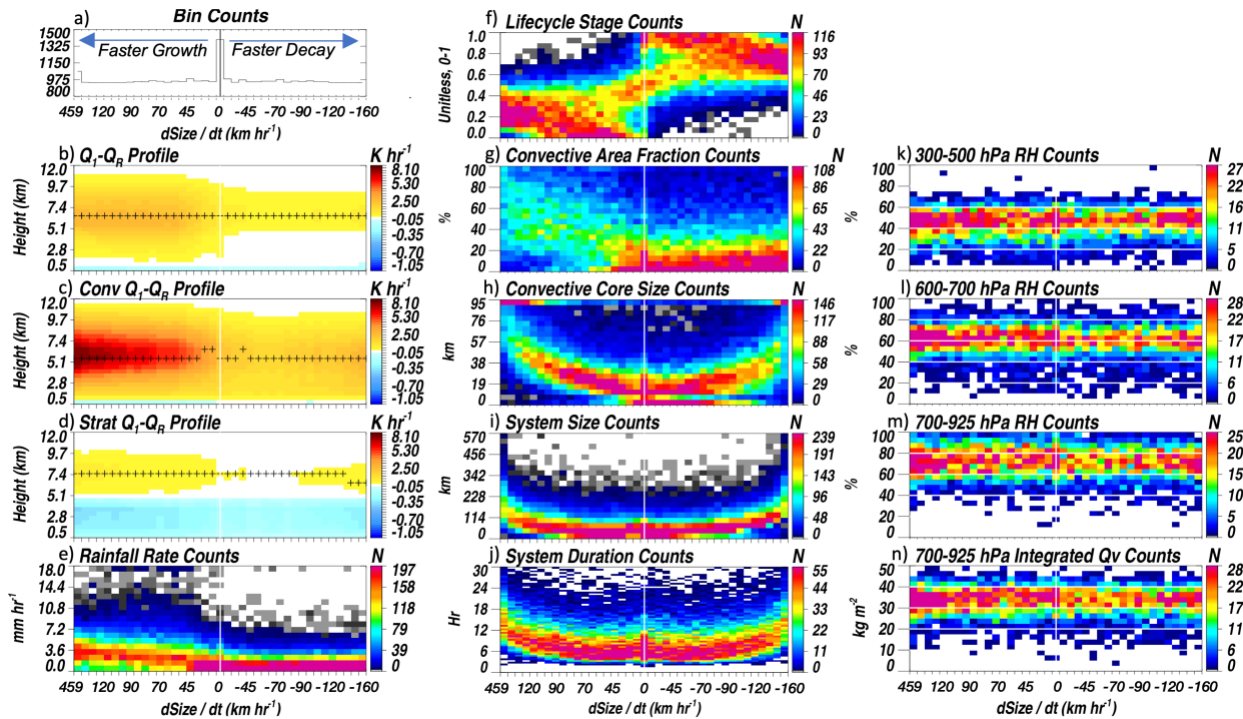
253 **Figure 4.** (a) Convective system maximum size as a function of lifetime, with the composite
 254 relationship overplotted as a solid line; (f) Early growth scatterplot (and solid line composite) as a
 255 function of lifetime. The remaining 8 panels show the composite system size evolution as a
 256 function of time for convective systems of varying lifetimes (solid black), with a random selection
 257 of 10 individual system evolutions overplotted for each lifetime panel (thin grey lines).

258

259 across durations (Fig. 4f; also similar to Feng et al., 2012), somewhat in contrast to Machado and
 260 Laurent (2004), though that study was limited to one regime and mostly focused on shorter-lived
 261 system relationships. This suggests that there is variability in the system size temporal evolution. A
 262 comparison of composite system evolutions and randomly-selected individual systems show that
 263 systems take different evolution trajectories (e.g., Figs. 4b-e, and g-j). While many systems reach
 264 their maximum at the temporal middle point of their lifecycle (as in Roca et al. (2017) and Feng et
 265 al. (2019)), the evolutions shown here suggest that some may grow slowly, then more quickly, or
 266 vice versa.

267 How should we understand the system trajectories? Regardless of whether cloud shield sizes
 268 systematically increase toward a maximum and decrease after, or whether the path toward and
 269 beyond a maximum is characterized by many ups and downs, both trajectories suggest substantial
 270 variability in actual cloud shield growth rates. Thus, we consider individual system trajectories as
 271 an accumulation of substantially varying instantaneous growth and decay sequences and aim to
 272 better understand the instantaneous growth rates themselves, assuming that the overall smooth
 273 composites emerge as the average of all individual trajectories.

274 3.2 Development of source – sink model for convective system cloud shield areas.



275 **Figure 5.** (left column) From top to bottom, bin counts, composite total, CSH convective and
 276 stratiform Q_1-Q_R profiles and surface rainfall rate histograms as a function of the cloud shield
 277 size rate of change. Total heating is averaged over the raining region, convective and stratiform heating
 278 profiles are averaged over their respective cloud type areas as in Fig. 3, and rainfall rate is a system
 279 average. (middle column) Various parameter histograms plotted as a function of the cloud shield
 280 size rate of change. (right column) As in the center column, but for Aqua/AIRS retrieved relative
 281 humidity (RH) for three different levels, and integrated water vapor in the lower troposphere. As
 282 in Fig. 2a-d, the plus symbols in the heating panels denote the altitude of peak heating. The white
 283 vertical lines denote the zero cloud shield size rate of change bin, and horizontal white lines in
 284 right column are added to aid in visual interpretation.

285
 286
 287 Fig. 5 shows MCS characteristics as a function of system growth and decay rates. Cloud
 288 shield size time tendency bin widths are objectively chosen so that approximately the same number
 289 of samples occur within each bin (symmetric about zero). It is clear that an asymmetry in growth
 290 and decay rates exists in Fig. 5a with the largest growth rate magnitudes exceeding the largest decay
 291 rate magnitudes. Because decay rates on average are much slower, a short-lived sequence of rapid
 292 growth has a large potential to extend the duration of a system cloud shield area. While difficult to
 293 infer from the composite lifecycle perspectives (Figs. 2 and 3), Fig. 5 suggests that growth in
 294 convective systems is strongly proportional to the convective area fraction (Fig. 5g) and convective

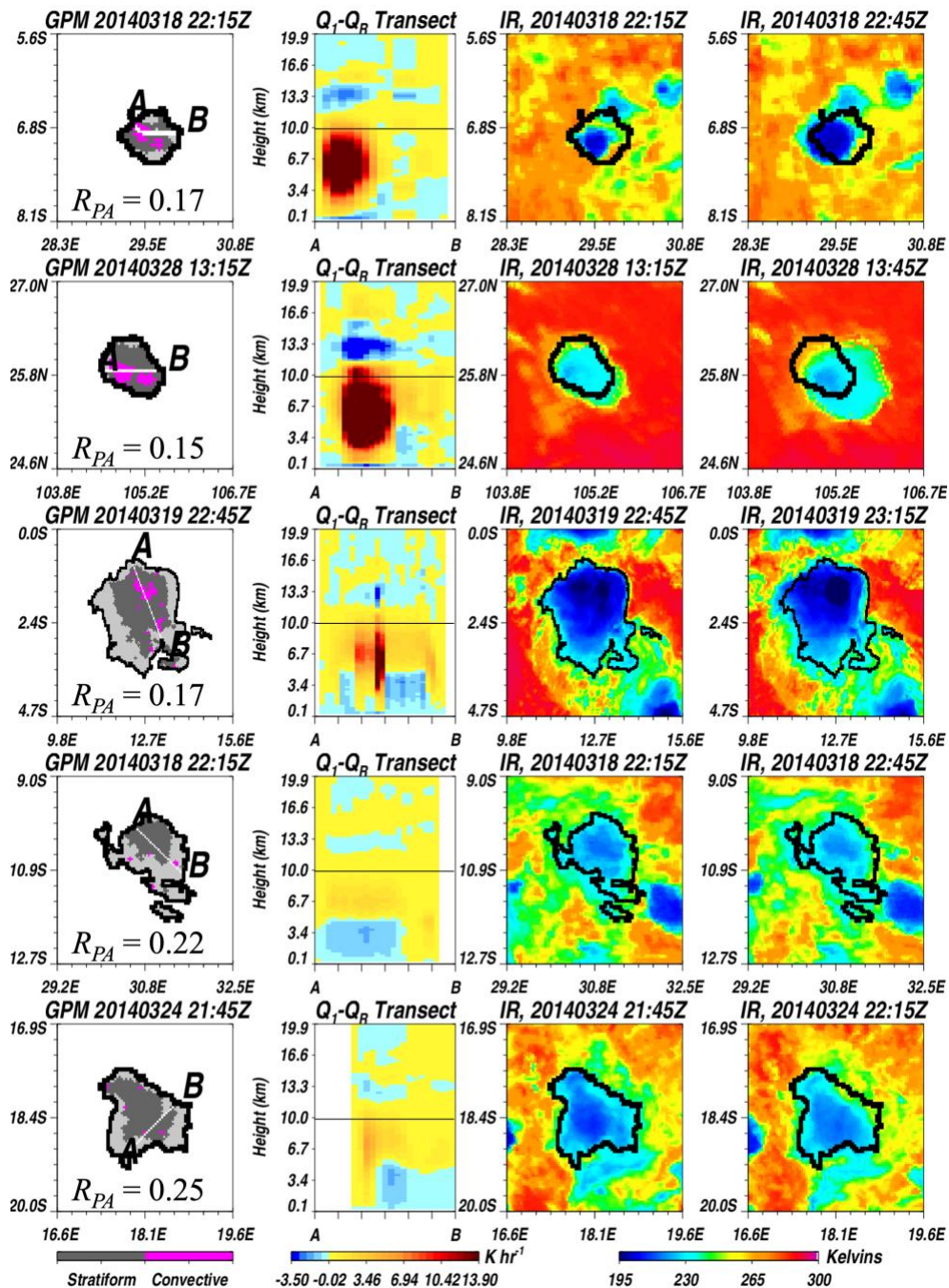
295 area Q_I-Q_R (or the vertical derivative of Q_I-Q_R above the melting level, since Q_I-Q_R tends toward
296 zero above 15 km). For simplicity, only CSH Q_I-Q_R is shown in Fig. 5; a repeat of analyses using
297 the SLH product yields similar interpretations. Is the state of convective cores themselves (Q_I-Q_R
298 structure, and size) during growth the dominant factor in growth rates and ultimately, duration?
299 Growth and decay broadly map to the first and last half of the lifecycles, respectively, but, consistent
300 with the individual system evolutions in Fig. 4, there is no one-to-one correspondence with life stage.

301 Nearly all of the largest system-average rainfall rates are found during system growth stages
302 (Fig. 5e). Since average rainfall peaks early in lifecycle composites (Fiolleau and Roca, 2013b; Feng
303 et al., 2019; Feng et al., 2021) and longer-lived systems contribute more to extreme precipitation
304 (Feng et al., 2018; Roca and Fiolleau, 2020), this may imply that rainfall extremes specifically occur
305 during growth periods of the early lifecycle stages. There is little relationship between growth and
306 decay rates, life stage (Fig. 5f), and moisture (Figs. 5k-n). PDFs of heating, sizes and durations, if
307 sorted according to the relative humidity (RH) at any level, also show little variation, so the
308 interpretation is consistent. It is worth noting that all of these RH values are much wetter than the
309 tropics-wide average implying that the existence of tropical MCSs (and their expansive raining cloud
310 shields) depends on humid conditions though actual system growth rates do not. Growth and decay
311 rates are inevitably tied to system duration (Fig. 5j), and a lack of relationship with moisture is
312 consistent with the weak role that saturation fraction plays in driving the specific onset time and
313 duration of heavy rainfall (Elsaesser et al., 2013).

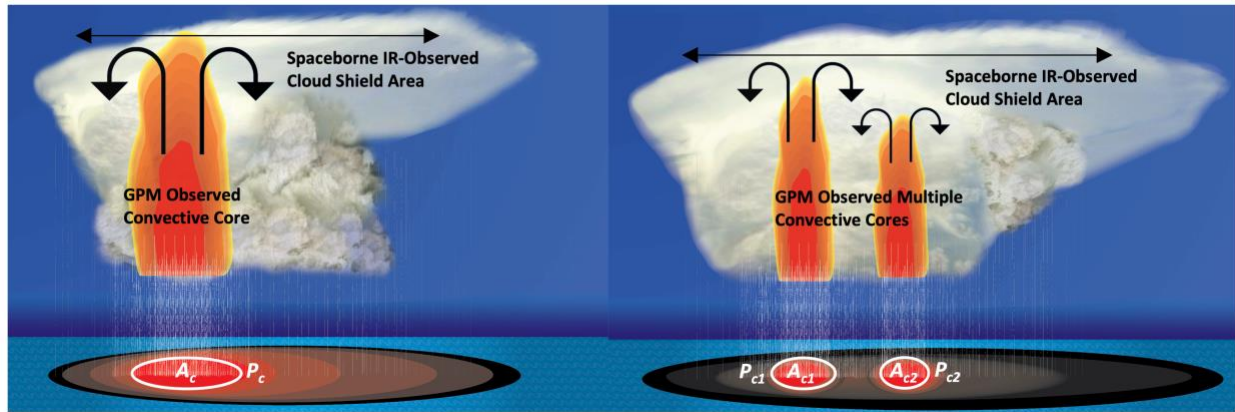
314 What is the cause of system cloud shield decay? It is less surprising that no relationship
315 between growth rates and moisture exists, particularly if cold pool – local environment interactions
316 (e.g., storm relative shear), gravity waves, sea breezes, or other small-scale factors are drivers of
317 upscale growth, though some studies suggest a moistening driven by previous convection (Rapp et
318 al., 2009; Mapes and Neale, 2011) may favor subsequent convection (which, in a Lagrangian
319 tracking sense, implies > 0 growth rates). For the decay portion of the spectrum, when convection
320 is absent or weak, if systems are not running into a drier environment, how do we determine why
321 systems decay? Among the clear signals that do manifest during decay: convective area is often
322 absent (Fig. 5h), or, if present, convective area fractions are often small (Fig. 5g), and decay rates
323 themselves are proportional to system size (Fig. 5i).

324

325



326 **Figure 6.** For different convective system examples (rows) over land, from left to right: co-located
 327 GPM convective-stratiform field (non-raining scene shaded in light grey, with the corresponding R_{PA}
 328 [see text and Fig. 7] shown for each system); CSH Q_I-Q_R profiles along the A – B transect; IR
 329 brightness temperature field at the time of the GPM overpass; and, IR brightness temperature field
 330 30 minutes after the GPM overpass. The black horizontal line near 10 km in the A – B transect
 331 panels denote the approximate 235 – 240 Kelvin temperature level (approx. threshold for cloud
 332 shield distinction). The solid black circular line in all panels of the 1st, 3rd and 4th columns does not
 333 change, and is used for visually gauging the changing IR cloud shield size.



334 **Figure 7.** Schematic of distributed convective cores in tracked convective systems, where to the left,
 335 convection is aggregated into one cell of area A_c and cell perimeter P_c , and to the right, the same total
 336 convective area is observed, but is split across two convective cells of differing areas (A_{c1} , A_{c2}) and
 337 cell perimeters (P_{c1} , P_{c2}). Since $P_{c1} + P_{c2} > P_c$, the ratio of the sum of convective cell perimeters to
 338 total convective area (i.e., referred to as R_{PA} in the text) increases as convective aggregation
 339 decreases (i.e., R_{PA} is larger for less convectively-aggregated system in right panel).

340

341 If system growth rates are related to the vertical derivative of convective Q_I-Q_R , then we can apply
 342 the concept of vertical convective mass flux convergence as a source for cloud shield area time
 343 tendencies (and thus, the magnitudes of growth rates), terms quantifiable using data from the current
 344 combination of satellite sensors in orbit. Fig. 6 shows two cases of rapidly growing cloud shields
 345 (top two rows) for systems characterized by strongly-heating convective regions and a third system,
 346 characterized by weaker convective Q_I-Q_R , whose shield is growing more slowly. The bottom two
 347 rows of Fig. 6 are examples of systems whose cloud shields are decaying. The decaying systems
 348 have little convection observed by GPM, and there is a sense that shield decay is slow and somewhat
 349 diffuse. These examples reflect the statistics shown in Fig. 5: growth can be rapid, and is likely
 350 associated with convection and a large vertical derivative of convective Q_I-Q_R . Decay is slower and
 351 occurs with a weakened convection area, or in many cases, occurs in the absence of a convective
 352 source, while being proportional to system size. Other interesting features in Fig. 6 include
 353 differences in the spatial aggregation of convective cells. For example, in the second row, convective
 354 area is very aggregated, while in the third row, the total convective area is nearly equivalent, though
 355 the area is now dispersed across numerous cells spanning the cloud shield. Cell aggregation can be
 356 quantified by computing the ratio of the sum of convective perimeters to total convective area
 357 (referred to as R_{PA} hereafter). R_{PA} is provided for each system example in the first column of Fig. 6.

358 The sum of convective perimeters was computed by adding up all edge 4-km GPM DPR pixels
 359 surrounding the GPM identified convective regions of the tracked convective system. As R_{PA}
 360 increases, convection becomes dispersed, i.e., more cells for a given area (see Fig.7 schematic for an
 361 illustration of systems with the same total cell area but different R_{PA}). How does R_{PA} relate to system
 362 growth rates?

363 Supported by the results thus far, and building on the conceptual MCS sustainability ideas
 364 previously proposed (e.g., Yuter and Houze, 1998; Schumacher and Houze, 2007; Futyan and Del
 365 Genio, 2007), an analytical model of the system cloud shield time tendency, with source terms driven
 366 by a temporal generation-of-convective-area term, vertical convective and stratiform mass flux
 367 convergence terms forcing lateral cloud shield expansion, and a sink term proportional to the cloud
 368 area, can be structured as follows:

$$369 \quad \frac{dA}{dt} \approx A_{c, \text{SRC}} - \frac{1}{\rho} \frac{dM_c}{dz} - \frac{1}{\rho} \frac{dM_s}{dz} - \frac{A}{\tau}, \quad (1)$$

370 where A is the cloud shield area, A_c is the convective area (with the subscript ‘SRC’ indicating this
 371 term represents the temporal generation of new convective area), M_c is the convective mass flux,
 372 M_s is the stratiform mass flux, ρ is the atmospheric density, and τ is a cloud shield area decay
 373 timescale. For comparison purposes, after moving the first term on the rhs of Eq. (1) to the lhs,
 374 the equation becomes one for the stratiform area time tendency, with the convective mass flux
 375 convergence term following Tiedtke (1993), Teixeira (2001) and follow-ons, and the decay term
 376 mimicking Hagos et al. (2020), although it is important to note that these terms were used in studies
 377 that were prognosing grid-box or fixed-domain stratiform *cloud fraction* or area changes whereas
 378 Eq. (1) prognoses *cloud physical area* changes following Lagrangian-tracked MCSs. Hagos et al.
 379 (2020) is further similar in that radar data (off the coast of Darwin, Australia) are used to develop
 380 a simple analytical model of stratiform area, though individual MCSs were not explicitly tracked
 381 in that analysis and the source terms vary in structure.

382 3.2.1 Constraining the Eq. (1) source term for convective area ($A_{c, \text{SRC}}$)

383 A_c at any given time is estimated by GPM though the time tendency is not, owing to the
 384 long GPM orbit re-visit period. However, it is likely unreasonable to assume that A_c is constant
 385 over the 30-minute TOOCAN database time step. Our goal is not to develop a new A_c
 386 parameterization (a topic worthy of a separate manuscript); we are merely aiming to isolate and

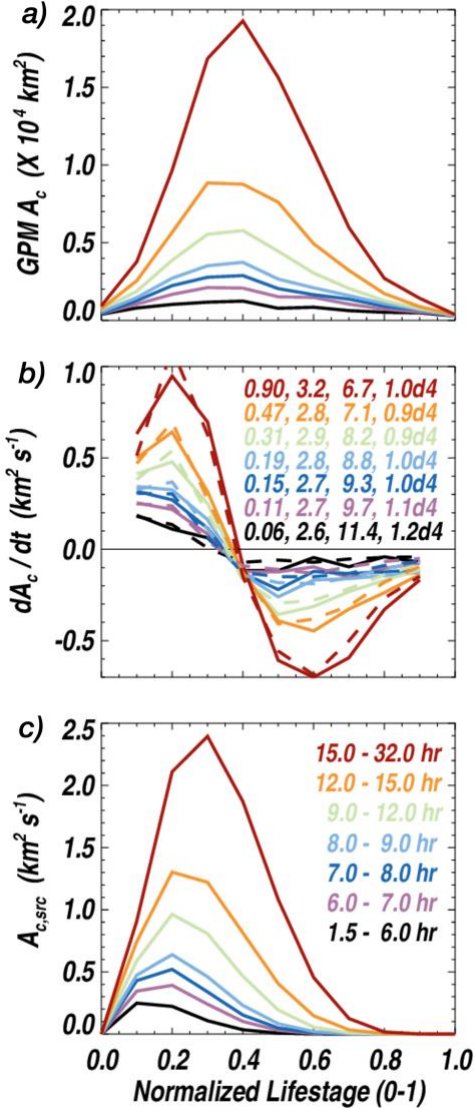


Figure 8. (a) Composite GPM convective area A_c as a function of system life stage (normalized by dividing system life stage hour by total duration). The A_c evolution is shown for different system durations (panel c shows duration legend). (b) Composite dA_c/dt as a function of normalized life stage (solid), with fits overlotted (dashed lines). The fit coefficients for the dA_c/dt model are color-coded by duration and provided in the following order: γ (km^2s^{-1}), α (unitless), β (unitless), and τ_{cs} (s). (c) The $A_{c, \text{SRC}}$ function used in the growth – decay rate model (see manuscript for discussion).

406 interval that characterizes the normalized life stage range. dA_c/dt can now be written as follows:

407

$$\frac{dA_c}{dt} \approx \frac{\gamma}{B(\alpha, \beta)} x^{\alpha-1} (1-x)^{\beta-1} - \frac{A_c}{\tau_{\text{cs}}}, \quad (3)$$

quantify the contribution to total cloud area by new convection area so that we can better describe the growth and decay rates of the stratiform cloud shield given the current state of convective towers. We proceed with a compositing technique to determine $A_{c, \text{SRC}}$. Analogous to the development of cloud area source – sink model, we assume the time tendency of A_c following the track of an MCS can be approximated as follows:

$$\frac{dA_c}{dt} \approx A_{c, \text{SRC}} - \frac{A_c}{\tau_{\text{cs}}}, \quad (2)$$

where τ_{cs} is the timescale for transition of convective cells to stratiform cells. A term representing evaporation of convective cells without a transition to stratiform is considered negligible within the moist MCS cloud envelope, though such a process could be inevitably wrapped into the computation of τ_{cs} . The average GPM A_c , plotted as a function of normalized life stage, is shown in Fig. 8a for varying system duration bins. From this, we can easily compute the composite dA_c/dt (solid lines of Fig. 8b) where dt is computed by multiplying the increment in normalized life stage by the system duration in seconds. We use a beta distribution to represent $A_{c, \text{SRC}}$, a function conveniently defined on the [0, 1]

408 where γ is a scaling factor, $B(\alpha, \beta)$ is the beta function with shape parameters ($\alpha, \beta > 0$), and x is
 409 the normalized life stage. With A_c , dA_c/dt and x being provided from our composite analyses (Fig.
 410 8), we use a Levenberg-Marquardt algorithm to solve for the unknown coefficients ($\gamma, \alpha, \beta, \tau_{cs}$).
 411 The fits to dA_c/dt are shown in Fig. 8b (dashed lines), with the coefficients also provided. The fits
 412 fully reproduce the observed composite dA_c/dt . Interestingly, τ_{cs} is nearly invariant across duration
 413 bins, with the timescale for conversion of convective cells to stratiform area being ~ 2.75 hr
 414 (coincidentally, this value falls within the deep-to-stratiform timescale range [0.5 – 3 hr]
 415 considered in Khouider et al., 2010). System durations of 6 – 10 hr are most common in the
 416 TOOCAN database, and for these systems, $A_{c, SRC}$ predicts that convective area is newly generated,
 417 early in the lifecycle (Fig. 8c), at a maximum rate of $\sim 0.5 \text{ km}^2 \text{ s}^{-1}$. Over the IR 30-min time step,
 418 this implies a generation of new convective area equivalent to a circle of diameter ~ 30 km.

419 Currently existing convective area A_c is assumed to transition to stratiform area, and a
 420 change in the cloud “type” does not result in a change in A . Thus, we must only account for
 421 generation of new convective area in Eq. (1), with no need for the second term of Eq. (2), and
 422 hence we substitute the computed $A_{c, SRC}$ functions (plotted in Fig. 8c) directly into the first term
 423 on the rhs of Eq. (1) to constrain convective area generation over the 30-min time step.

424 3.2.2 Reformulating and constraining the Eq. (1) vertical mass flux convergence terms

425 Bony et al. (2016) and Seeley et al. (2019) explored the convective mass flux
 426 convergence term (equivalent to net detrainment) as it relates to understanding tropical cloud
 427 fraction sources. Using Weather Research and Forecasting (WRF) simulations, Seeley et al.
 428 (2019) found that net detrainment did not explain the altitude of peak cloud fraction. However, it
 429 is also evident in Seeley et al. (2019) that for cloud fraction profiles above ~ 10 km, where
 430 entrainment is minimal, convective source formulations represented as net or gross detrainment
 431 yield similar results. Such altitudes are closer to the IR-observed MCS cloud tops, and thus, a net
 432 detrainment formulation for the convective source term in our analysis is reasonable. The
 433 detrainment term can be re-cast in terms of $Q_I - Q_R$, allowing us to assess this formulation globally
 434 across the tropics using GPM $Q_I - Q_R$ mapped to MCS shields. For any system, M_c is equivalent to
 435 $\rho A_c w$ (where w is the vertical wind speed averaged over A_c); but, M_c is not observable from GPM
 436 since vertical motion is not among those parameters retrieved. From the budget equation for dry
 437 static energy ($s = c_p T + gz$, where c_p is the specific heat at constant pressure, T is the temperature,

438 and gz is the geopotential), if we assume small temporal changes in dry static energy (Sobel et al.,
 439 2001) across A_c , a small horizontal advection term, and assume convective Q_I-Q_R dominates over
 440 radiative heating within the convective cells, we can approximate w as follows:

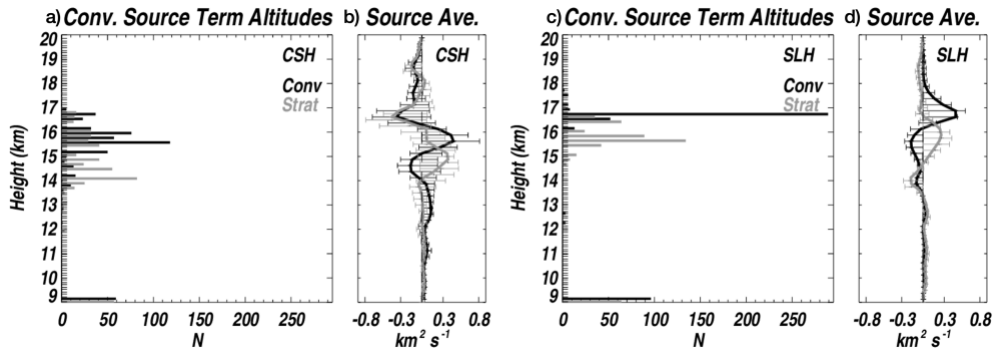
$$441 \quad w \approx \left(\frac{1}{c_p} \frac{ds}{dz} \right)^{-1} (Q_I - Q_{R_{\text{Conv}}}) = \left(\frac{1}{\Gamma - \Gamma_d} \right) (Q_I - Q_{R_{\text{Conv}}}), \quad (4)$$

442 where Γ is the average temperature lapse rate across A_c (and subscript d on Γ denotes the dry
 443 adiabatic lapse rate) and Q_I-Q_R is in units of K s^{-1} . A_c profiles are not provided by GPM (i.e.,
 444 convective classification is independent of height) yet a spectrum of convective cells of varying
 445 vertical depths likely exists across A_c . Thus, as altitude increases and convective area fraction
 446 systematically decreases (Kumar et al., 2015; Giangrande et al., 2016), w computed here might
 447 best be thought of as an approximate vertical motion across A_c that likely includes increasing
 448 contribution from non-convective motions above the tops of shallower or upward growing
 449 convective towers (as opposed to w representing convective core vertical updraft speeds at all
 450 altitudes, specifically). With Eq. (4), the second term on the rhs of Eq. (1) can now be
 451 approximated as follows:

$$452 \quad - \frac{1}{\rho} \frac{dM_c}{dz} \approx - \frac{A_c}{\rho} \frac{d}{dz} \left(\rho \frac{Q_I - Q_{R_{\text{Conv}}}}{\Gamma - \Gamma_d} \right). \quad (5)$$

453 The third term on the rhs of Eq. (1) can be written like Eq. (5), except with A_c and convective Q_I-
 454 Q_R being swapped for the stratiform counterparts. We explore inclusion of this third term in Eq.
 455 (1) since the mesoscale divergence near the tops of well-developed precipitating stratiform regions
 456 might be significant enough to force an observable lateral expansion of the entire cloud shield.

457 We use the satellite retrievals discussed in section 2 to populate the two source terms and
 458 plot statistics in Fig. 9. The satellite sounder retrievals of temperature are characteristic of non-
 459 cloudy unsaturated tropical environments outside of the tracked systems. Thus, to define Γ at all
 460 altitudes within any system cloud shield, we assume the atmosphere is saturated and assume a
 461 moist adiabatic lapse rate (hereafter, Γ_m) whose magnitude is set to the climatological AIRS grid
 462 box Γ_m closest to the tracked system. Since Γ_m varies strongly with temperature, this gives
 463 regionally varying lapse rates. For both the CSH (Fig. 9a,b) and SLH (Fig. 9c,d). products, the
 464 convective source terms maximize $\sim 1 - 2$ km above the stratiform sources. Because of this, the



465 **Figure 9.** For the CSH product, (a) the height distribution of the maximum value of the cloud area
 466 tendency convective source term, and (b) the composite-average source term profile (horizontal
 467 lines depict the $\pm 1\sigma$ range). (c and d): as in a and b, but for the SLH product.

468

469 stratiform source terms at lower altitudes would influence the vertical cloud extent and
 470 cloud area tendency profile below the cloud top. Thus, the downward-looking two-dimensional
 471 GEO-IR satellite perspective will yield a cloud shield tendency largely driven by the convective
 472 mass flux term, and so we simplify Eq. (1) further by neglecting the stratiform source term. Fig.
 473 9 suggests large differences in the altitudes of peak cloud area tendencies derived from CSH and
 474 SLH. The altitude of the peak source is > 1 km higher in SLH than that inferred from the CSH
 475 product. For SLH, the convective and stratiform terms combined suggest a cloud fraction profile
 476 that would peak from 16 – 17 km (Fig. 9c,d), which is 1 – 2 km higher than observed (see Seeley
 477 et al., 2019). Therefore, in addition to neglecting the stratiform mass flux term, we use the CSH
 478 heating product for the remainder of the paper to quantify the magnitude of the convective source
 479 term. Additionally, the magnitude of this convective mass flux term is set to the profile maximum
 480 above 9 km (i.e., at or above the IR-identified altitude for cold “cloud shield” coverage) in the
 481 following analyses.

482 3.2.3 Final discretized equation for predicting the cloud shield area growth and decay rates.

483 Regarding the final term of Eq. (1) (the sink term, the last term on the rhs), dissipation of
 484 cloud area A depends on total ice condensate within cloud. GPM products do not provide all ice
 485 condensate species (not to mention the difficulty that exists in retrieving cloud ice accurately
 486 (Duncan and Eriksson, 2018)). Sources of ice include convective ice detrainment and saturated
 487 ascent in the stratiform/anvil region, with sinks being driven by precipitation. Convective and
 488 stratiform latent heating and precipitation terms could be used to partially infer ice condensate if
 489 the evolution of these terms along system paths were known; however, GPM provides these

490 estimates at one instant, and though GPM estimates could constrain the current perturbation to
 491 total ice condensate within cloud, total ice condensate itself is not. Additionally, since evaporation
 492 is slow and inefficient in the cold upper troposphere (Seeley et al., 2019), mixing near cloud edges
 493 may actually act to increase cloud area if the ice condensate amount near cloud edges is large
 494 enough. These processes are all wrapped into the decay timescale τ of the Eq. (1) sink term.

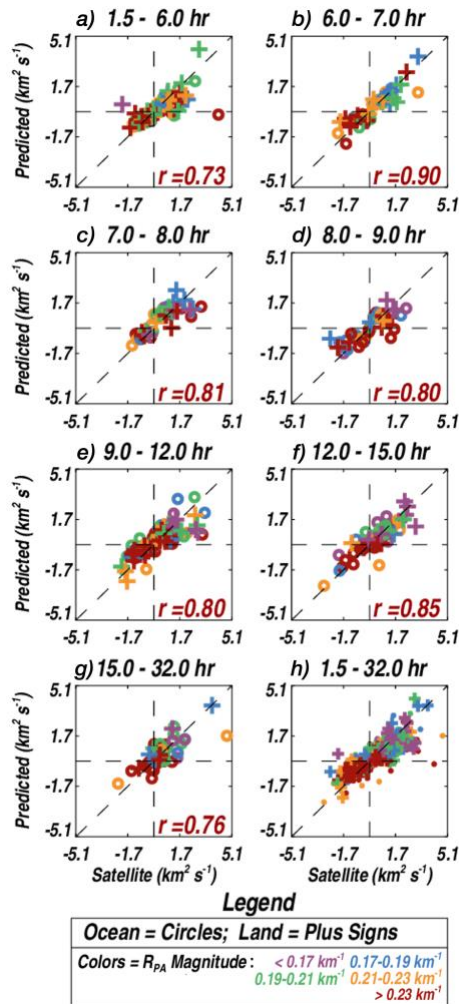
495 With $A_{c, SRC}$ now constrained (section 3.2.1) and with reformulation of the convective mass
 496 flux term (section 3.2.2), we re-cast the cloud shield area time tendency Eq. (1) as a regression
 497 equation with the terms discretized as follows:

$$498 \quad \frac{\Delta A}{\Delta t} = A_{c, SRC} - C_1 A_c \times \max \left[\frac{1}{\rho} \frac{\Delta}{\Delta z} \left(\rho \frac{Q_I - Q_{RCConv}}{\Gamma_m - \Gamma_d} \right) \right] - C_2 A, \quad (6)$$

499 where $\Delta A/\Delta t$ is explicitly provided by TOOCAN ($\Delta t = 30$ min), C_1 accounts for possible satellite
 500 retrieval limitations in quantifying the vertical profile of convective area and in-cloud lapse rates,
 501 C_2 is equal to τ^{-1} , and $\max[\dots]$ refers to a search of the maximum of the enclosed term above 9km,
 502 as discussed in 3.2.2. We apply Eq. (6) to MCS data binned by convective system duration and A
 503 time tendencies, solve for C_1 and C_2 , and evaluate the model A time tendencies. The A time
 504 tendency bin widths ($\sim 0.15 \text{ km}^2 \text{ s}^{-1}$) are chosen so that compositing artifacts are minimized while
 505 ensuring each bin has at least one GPM sample. We apply the model to all data combined, and to
 506 data in different duration bins separately (using the same bins shown in Fig. 8c) in large part to
 507 test the robustness of the model across different system types and subsets of data.

508 3.3 Growth and decay rates stratified by surface type, system duration and convective organization

509 The observed and model-predicted dA/dt are shown in Fig. 10 for storms of varying
 510 durations (the results for all data combined, independent of duration, is shown in Fig. 12a). Fig.
 511 10 points are coded according to whether the system was over ocean (circles) or land (pluses) and
 512 colored according to R_{PA} . The fact that most points fall close to the 1:1 line suggests that the
 513 functional form of the cloud shield model is skillful across the spectrum of convective system
 514 duration bins and aggregation states. Interestingly, the computed regression coefficients (C_1 and
 515 C_2) are largely duration independent, with $C_1 \sim 1$ and $C_2 \sim 0.00018 \text{ s}^{-1}$. That C_1 is nearly unity for
 516 each duration bin suggests that the mass flux convergence source term formulated in terms of
 517 diabatic heating and moist adiabatic lapse rates is a good approximation, with C_1 not needed. With
 518 C_2 having units of s^{-1} , this implies that the IR cloud shield decay timescale is 1 – 2 hr. Seeley et



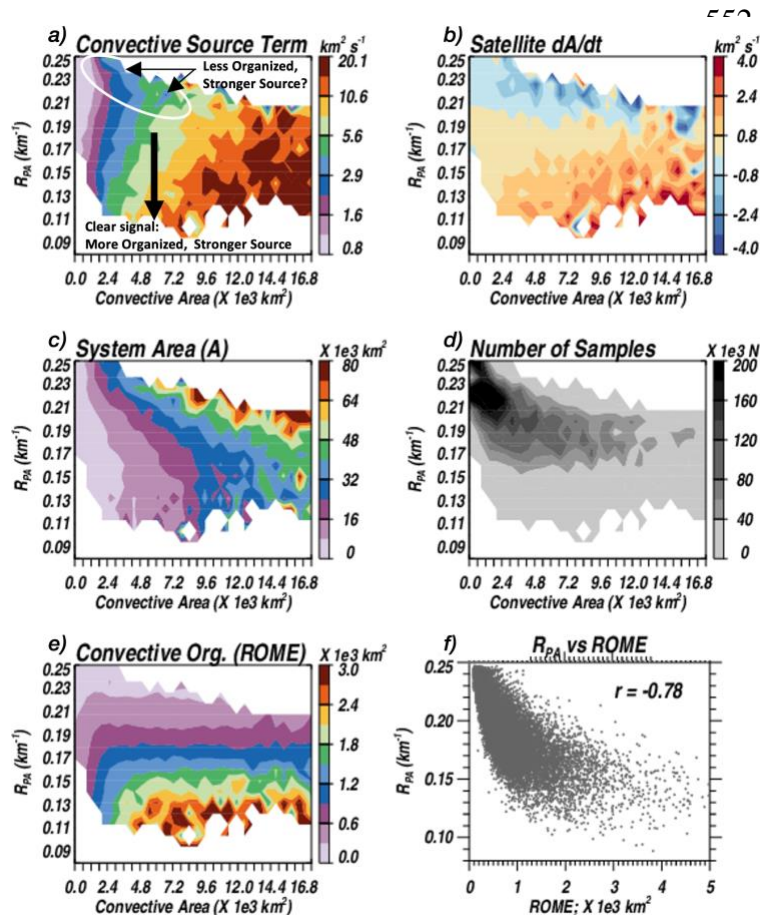
al. (2019) using model simulation experiments derived global ice cloud lifetimes of $\sim 5 - 10$ hr at $10 - 15$ km, with a decrease in the lifetime as altitude increases further, while Hagos et al. (2020) derived a decay timescale of 7 hr for stratiform areas. These decay timescales were computed for convection in aggregate or global cloud analyses as opposed to tracked MCS, and thus the timescale are not apples-to-apples comparable. Since the MCS cloud shields tracked in TOOCAN are likely raining at rates larger than average convective scenes, one might expect that the decay timescales are shorter since precipitation could be a stronger sink of stratiform cloud area.

Fig. 10 does not suggest a larger systematic deviation from the 1:1 line in the predictions for systems over land relative to those over ocean. As mentioned in section 3.1, convection is known to be more intense over land than ocean. The Eq. (5) convective source term yields a source magnitude that peaks near 16.5 km over land and 15.5 km over ocean,

Figure 10. Predicted dA/dt versus satellite estimated dA/dt for different convective system duration bins, with the plot symbol denoting surface type (ocean = circles, land = plus signs) and symbol color denoting the R_{PA} magnitudes. Correlation coefficients for the prediction vs. observation are shown at the bottom of each panel. The last duration range panel shows all points combined for additional visual comparison across all duration bins.

537 with the source itself a factor of ~ 2.5 stronger over land than ocean on average ($0.8 \text{ km}^2 \text{ s}^{-1}$ and 2.0
 538 $\text{km}^2 \text{ s}^{-1}$ for ocean and land, respectively). These results are consistent with land – ocean differences
 539 in convection, with the increased land source attributed to stronger diabatic heating and a larger
 540 vertical gradient in diabatic heating instead of being attributed to moist adiabatic lapse rate
 541 differences (not shown). Additionally, departures in the prediction from the 1:1 line do not seem to
 542 be dependent on cell aggregation (i.e., R_{PA}). This result is interesting, particularly in light of Hagos
 543 et al. (2020) where it was found that if there were more convective cells for a given convective area,

544 growth of the stratiform area was larger. The Hagos et al. (2020) result was interpreted within the
 545 context of the “particle fountain” idea proposed by Yuter and Houze (1995), where if convective
 546 cells were more scattered like trees in a forest, their ice particles were more likely to fall outside of
 547 the existing convective area, thus favoring growth of stratiform cloud regions. For a given
 548 convective area, as the number of convective cells increases, the sum of the perimeters surrounding
 549 convective cells increases (Fig. 7); therefore, growth of the stratiform region (or cloud shield area in
 550 this study, given the correlation with stratiform area) should be larger as R_{PA} increases. Since the
 551 source – sink model does not specifically consider convective perimeters, the lack of outliers in the



prediction might be surprising.

We investigate this further in Fig. 11a, where the convective source term (i.e., Eq. 5) is plotted as a joint function of convective area A_c and R_{PA} . R_{PA} is one way to quantify convective aggregation, but this metric is also strongly correlated with an independent convective “organization” metric (i.e., the Radar Organization Metric or ROME; Fig. 11f) following Retsch et al. (2020) which specifically defines organization based on the size and proximity of convective cells. As defined here, organization increases as ROME

Figure 11. (Left column) From top to bottom, the average convective source term (Eq. 3 in manuscript), average convective system IR-estimated cloud shield area, and average organization of convective cells (defined using the Radar Organization Metric, or ROME, as in Retsch et al. 2020) as a joint function of total convective area (A_c) and the ratio of the sum of convective cell perimeters divided by total convective area (R_{PA}). (Right column) As in left, but for (b) satellite estimated system area time tendency (dA/dt) and (d) number of samples contributing to composites. Panel f illustrates the relationship between R_{PA} and a convective organization diagnostic (ROME).

569 increases, with the upper limit of organization being equivalent to the mean convective cell area
 570 multiplied by 2. Fig. 11e shows how ROME increases as R_{PA} decreases for the same convective
 571 area. As expected, Fig. 11a shows that the convective source term increases as A_c increases (and,
 572 indeed, the total satellite cloud shield time tendency in Fig. 11b follows this pattern). Additionally,
 573 there is a very clear pattern showing an increase in the convective source term as R_{PA} decreases.
 574 Interestingly, this tendency reverses when the cloud shield area is undergoing decay on average. In
 575 this state, as R_{PA} increases (i.e., organization decreases), the source term also increases (top left
 576 portion of Fig. 11a). The latter result is similar to the findings of Hagos et al. (2020). Might this
 577 imply that less organized convection during the later decaying stages of system lifecycles favors
 578 cloud shield sustenance and increased longevity? At first glance, this seems to be a small portion of
 579 the data state space; however, this region of the state space comprises large cloud shield areas and
 580 system counts (roughly 20-25% of the data lie above the white-outlined area in the top left panel of
 581 Fig. 11). In summary, even though Eq. (6) does not specifically consider convective cell
 582 aggregation, there is a signal in the vertical (associated with the convective cell-ensemble Q_I-Q_R
 583 height derivative) that is serving as a strong enough proxy to modulate variations in the cloud area
 584 source as convective cell organization changes, which is probably why Fig. 10 shows no clear biases
 585 in the prediction as cell aggregation varies.

586 With $A_{c,SRC}$ moved to the lhs of Eq. (6), an anvil cloud shield growth rate equation can be
 587 developed (the full anvil is not captured, of course, since the thinner parts of the anvil are likely not
 588 detected in the TOOCAN database). Though necessary for development here, in a climate model,
 589 $A_{c,SRC}$ would be irrelevant, with convective area being determined by the model's own convective
 590 parameterization. Thus, in a model, anvil area growth rate could be predicted based on the
 591 convective diabatic heating structure, model A_c , temperature lapse rates, and use of C_2 as derived
 592 here (where C_2 can be a fixed, based on results presented, though the processes that govern its
 593 magnitude requires additional investigation). It is obvious that in order for the anvil growth rate to
 594 be ≥ 0 (i.e, the stratiform/anvil area is sustained or growing), term 2 must be \geq term 3 on the rhs of
 595 Eq. (6). If we re-arrange these terms, set C_1 to unity (as discussed), and solve for the convective area
 596 fraction necessary for stratiform anvil sustenance, we arrive at the following equation:

$$597 \quad \frac{A_c}{A} \geq C_2 / \max \left[\frac{1}{\rho} \frac{\Delta}{\Delta z} \left(\rho \frac{Q_I - Q_{R_{Conv}}}{\Gamma - \Gamma_d} \right) \right], \quad (7)$$

598 where all parameters have been previously introduced. With C_2 fixed at 0.00018 s^{-1} , an analysis of
 599 the $\max[\dots]$ term (considering all data combined across durations) suggests the convective area
 600 fraction must exceed ~ 0.2 in order for the stratiform component of the shield to grow, with the
 601 growth rate magnitude itself dependent on A_c and the vertical gradient of diabatic heating and lapse
 602 rates.

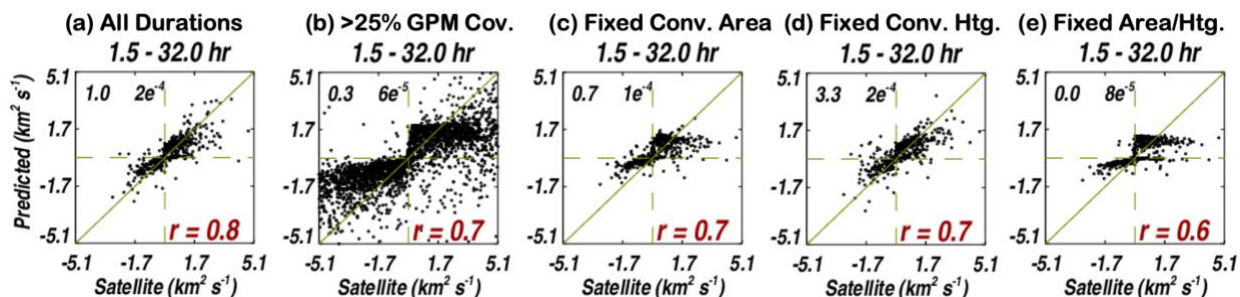
603 3.4 Sensitivity of source – sink model to structure and assumptions

604 Developing a suitable equation for $A_{c,SRC}$ is necessary for determining the structure and
 605 coefficients that drive cloud area expansion, though $A_{c,SRC}$ itself, by design, is largely empirical. This
 606 is because our focus is on how stratiform anvil areas change given the current structure of convection
 607 in a given system, and not on what drives changes in the convective cores themselves. We have
 608 tested different functions for deriving $A_{c,SRC}$. Most perform poorly when compared to the GPM A_c
 609 composites (Fig. 8a), and that is because few functions can reproduce the beta distribution shape that
 610 allows for capturing the sharp increase in A_c production during system growth, quick decay toward
 611 the middle life stages, and no production of A_c during later life stages. Originally, we did assume a
 612 constant (or ‘average’) $A_{c,SRC}$, but this led to C_1 and C_2 varying with system duration (though the
 613 averages of those two coefficients across all durations were close to the estimates found here). We
 614 attribute the variation due to systematic differences in sampling of life stages across system durations.
 615 For the shorter-lived (smaller) systems, the GPM swath width often permits a view of systems at
 616 random life stages; for the longer-lived (larger) systems, there is a skewing towards earlier life stages
 617 since the largest systems reach peak size later, and their expansive cloud shields by then are under
 618 sampled by GPM (and not included in our analyses). Since $A_{c,SRC}$ peaks during early stages (Fig.
 619 8c), assuming a constant $A_{c,SRC}$ across the entire lifecycle underestimates the production occurring
 620 during early stages often-sampled for longer-lived systems, whereas for the shorter systems,
 621 assuming a constant $A_{c,SRC}$ leads to a better result since the underestimation of A_c production earlier
 622 is cancelled by the overestimation later. This systematic shift in $A_{c,SRC}$ estimation is compensated by
 623 a corresponding systematic change in C_1 and C_2 as system duration increases.

624 The above discussion motivates the following question: how do our GPM sampling
 625 requirements influence our quantitative results? Over 90% of the time when the predicted minus
 626 satellite estimated differences exceed $1 \text{ km}^2 \text{ s}^{-1}$, the MCS cloud shield area was under-sampled by
 627 GPM. As mentioned in section 2.1, at least 2/3 of the convective system cloud shield area must be

628 sampled by GPM in order for the data point to be included in development and analysis of the
 629 analytical model. Convection occupies a small fraction of a cloud shield, and therefore, it is easy for
 630 GPM to completely miss convective cores. This limitation is not resolved by simply increasing the
 631 size of our database. Instead, this is the result of system sizes often exceeding the swath width of
 632 the GPM DPR orbit, and no sample size will ever permit 2/3 sampling of large MCS shields (Nesbitt
 633 et al., 2006; Fiolleau and Roca, 2013b).

634 While decreasing the 2/3 coverage threshold drastically increases the sample count, there is
 635 a price to pay. If convection is missed too often, the convective mass flux source term is artificially
 636 zero too frequently. This issue does not simply lead to more scatter in any one duration bin. Instead,
 637 with a weaker (or zero) source term, a weaker sink term would also be computed to achieve the best
 638 fit to the ensemble of points, and subsequently, the sensitivity of the prediction is lower. This is
 639 depicted as a “flattening” in the prediction. Conversely, a more conservative threshold (e.g., 90%
 640 coverage), while increasing the probability that convective cores are sampled, results in almost no
 641 data being available no matter the record length (and for systems that are sampled, their sizes are
 642 often small, since smaller shields are the ones entirely viewable by GPM). Thus, the 2/3 threshold
 643 strikes a balance between data samples and system sizes, and the necessity of sampling the
 644 convective source. To assess the under-sampling issue further, one fit is re-computed independent
 645 of duration bin (Fig. 12a), which clearly resembles all results in the Fig. 10 panels, while another fit



646 **Figure 12.** Like Fig. 10, except with varying thresholds used for constraining the convective
 647 source term in the cloud shield area time tendency equation and no coding of points based on
 648 surface type (land, ocean) or convective organization. From L to R: (a) fits calculated independent
 649 of duration bin; (b) calculations performed with less stringent GPM coverage required (>25% of
 650 the system shield must be sampled); (c) calculations performed while fixing the convective area
 651 to the average across all systems; (d) calculations performed while fixing the convective heating
 652 profile to the average across all systems; and, (e) calculations performed while fixing both
 653 convective area and convective heating profiles to the average across all systems. For each panel,
 654 the C_1 and C_2 coefficients determined from the model fitting are plotted (see manuscript for further
 655 discussion).

656 is recomputed after requiring only 25% of the area to be covered by GPM (Fig. 12b). Clearly, the
657 relationship is not as strong with less sampling of the convective structures, and both growth and
658 decay rates are further underestimated, with a flattening in the prediction observed.

659 Is the vertical convective heating structure or convective area the key component driving the
660 convective mass flux source term? As a test for system convective core similarity, we swap the
661 mean convective area across all systems for the actual observed convective area and re-compute the
662 fit. Note the poorer fit for this experiment in Fig.12c, particularly when the satellite data indicates
663 the systems are growing. In Fig. 12d, the all-system-average convective heating profile is substituted
664 in, and Fig. 12e shows the results when there is no variation in convection across systems (i.e., mean
665 convective area and mean heating profile are used). That Fig. 12d looks like Fig. 12a suggests that
666 capturing the convective area, via sampling of a large-enough fraction of the system, is most
667 important. In the Fig. 12d experiment, C_I (though previously equal to 1) becomes a scale factor on
668 convective area (whose magnitude was already influenced by the average vertical derivative of Q_I -
669 Q_R and temperature lapse rates in this experiment). Importantly, Fig. 12d suggests that one could
670 simply use some constant times A_c as the source term of the model, and never consider information
671 about Q_I - Q_R nor temperature lapse rates as we have. In such a case, the computed C_I coefficient
672 would be $\sim 0.0008 \text{ s}^{-1}$. Of course, the following question would then arise: where does the arbitrary
673 0.0008 s^{-1} derive from? Clearly then, the advantage of using the convective mass flux source term
674 (Eq (6), second term on rhs) as we have formulated it, instead of some constant multiplied by A_c in
675 a new source term, is that it provides an understanding of the source term physics that clearly tie to
676 the vertical gradient of convective diabatic heating in systems, co-incident with an increasingly stable
677 upper troposphere, which act as pre-factor for determining the quantitative role that convective area
678 plays in cloud shield growth rates.

679 **4 Conclusion**

680 How tropical anvil areal extent will change and modulate radiation as the climate warms is
681 one of the largest uncertainties in recent cloud feedback assessments (e.g., Sherwood et al., 2020),
682 and improved understanding of the spectrum of deep convective system areal extents, how system
683 areas couple with convective and stratiform diabatic heating, and the construction of simple models
684 that can inform GCM convective parameterization is needed. In this work, we specifically focused

685 on increasing our understanding of MCS cloud shield area time tendencies and relationship with
686 convective heating.

687 Composite analyses show that longer-lived (and larger) deep convective system cloud shields
688 are associated with increased diabatic heating above the melting level (Figs. 2 and 3), largely due to
689 stratiform region heating. The system evolution composites are not necessarily representative of
690 individual system evolutions, though (e.g., Fig. 4). Instead, evolutions may be best thought of as
691 collections of instantaneous bursts in growth mixed with sequences of decay, such that a longer-
692 lived duration may arise from a fortunate series of growth sequences. Results suggest that the growth
693 of a convective system shield is strongly related to generation of convective area and a strong vertical
694 gradient of convective-region heating (computed from its peak above the melting level to the cloud
695 top) forcing lateral cloud growth (Fig. 5). Decay rates are strongly related to the instantaneous size
696 of the cloud shield itself, but exhibit no clear dependence on relative humidity.

697 A simple convective-source, slow-decay model (Eqs. 1 and 6) informed by the observational
698 results is developed. Since satellite-estimated vertical winds in convection are not available for
699 developing the cloud shield model source term, the model is re-formulated in terms of diabatic
700 heating, an advantage that permits analyses via use of GPM retrieved diabatic heating mapped to
701 MCSs (and which has an analog in GCM output since most convective parameterizations yield
702 diabatic heating profiles). The remaining model terms are quantified using satellite retrievals from
703 GEO-IR, AIRS/MLS and convective area estimates from GPM, and uncertain or unknown
704 coefficients are derived by applying the model to all tropical (land and ocean) scenes and duration
705 bins. The simple cloud shield model often explains over 60% of the 30-min changes in cloud shield
706 areas across the global tropics (with comparable skill across MCS duration bins, and no clear biases
707 for land or ocean systems nor convective cell aggregation). There is a rich structure in the cloud area
708 source term that varies as a function of convective cell organization, with overall, the source term
709 increasing with convective organization, while for decaying shields characterized by smaller
710 convective area overall, the source term sometimes increases as organization decreases. Results
711 further suggest that convective and stratiform rainfall and associated diabatic heating are often
712 coupled, stratiform heating is present at all system life stages past initiation (Fig. 3), and stratiform
713 area is continually produced along the path of the MCS (Eq. 1). Thus, the “convective to stratiform
714 transition” onset period might also be considered an emergent property, useful for evaluating output

715 from a GCM at the grid box and timestep-scales during parameterization development, as opposed
716 to a process that happens abruptly or at a fixed life stage.

717 Toward understanding the distribution of convective system durations, work is underway to
718 understand factors favoring convective area maintenance and/or re-generation following the path of
719 a system so as to understand the functional form of $A_{c,src}$ and to understand its variation across
720 systems of varying duration. Extending the Lagrangian analyses to three-dimensional MCS cloud
721 volumes via analyses of height-resolved cloud fractions alongside the stratiform area source term,
722 exploring the role of radiative heating (Gasparini et al., 2019) in cloud shield time tendencies, and
723 understanding how stratiform precipitation sinks, vertical wind shear, and organization metrics
724 conspire to set the magnitude of the cloud shield decay term timescale τ are other avenues being
725 pursued. An overall objective is to provide improved process-level understanding and useful
726 observational depictions for improving the representation of convection in parameterized GCMs
727 tasked with providing projections of 21st century climate, the reliability of which depends on
728 accurately representing the spectrum of cloud feedbacks (Hartmann and Larson, 2002; Zelinka and
729 Hartmann, 2010, 2011; Bony et al., 2015), including the role of organized convection (Moncrieff,
730 2019) and convection-driven high cloudiness.

731

732 *Acknowledgements*

733 Computing resources for data analysis were provided by the NASA High-End Computing
734 (HEC) Program through the NASA Center for Climate Simulation (NCCS) at the Goddard Space
735 Flight Center. This research was supported by the Precipitation Measurement Missions program
736 (RTOP WBS #573945.04.18.03.60), the Terra, Aqua, and Suomi NPP program (Grants
737 #80NSSC18K1030 and #80NSSC21K1978), and the NASA Data for Operation and Assessment
738 program (Grant #NNX17AF46G). All data used for analysis and analytical model development
739 are available in the public domain. The TOOCAN convective system tracking database is
740 available at <https://toocan.ipsl.fr/toocandatabase/>. The GPM CSH and SLH Q_I - Q_R , rainfall and
741 convective-stratiform pixel identification are available from NASA's Goddard Earth Sciences
742 Data and Information Services Center (GES DISC) at
743 https://gpm1.gesdisc.eosdis.nasa.gov/data/GPM_L2/, while AIRS V6 water vapor Level 2 data
744 mapped to MCSs are available from GES DISC at

745 https://disc.gsfc.nasa.gov/datasets/AIRS2RET_006/summary/. AIRS V6 and MLS V3 gridded
746 (Level 3) datasets used for computation of climatological moist adiabatic lapse rates are available
747 from the Observations for Model Intercomparison Project (Obs4MIPS) archive hosted on the Earth
748 System Grid Federation at <https://esgf-node.llnl.gov/projects/obs4mips/SatelliteDataProducts>.
749 We thank Niki Barolini for the design of Figure 7. Helpful comments by external referees provided
750 on an earlier manuscript submitted for review are acknowledged, and we thank Prof. Courtney
751 Schumacher and two anonymous reviewers for their comments and constructive feedback, which
752 improved this manuscript.

753

754

755

756

757

758

759

760

761

762

763

764

765

766

767

768

769

770

771
772
773
774
775
776
777
778
779
780
781
782
783
784
785
786
787
788
789
790
791
792
793
794
795
796

REFERENCES

Bony, S., B. Stevens, D.M.W. Frierson, C. Jakob, M. Kageyama, R. Pincus, T.G. Shepherd, S.C. Sherwood, A.P. Siebesma, A.H. Sobel, M. Watanabe, and M.J. Webb, 2015: Clouds, circulation and climate sensitivity. *Nature Geosci.*, **8**, 261-268.

Bony, S., B. Stevens, D. Coppin, T. Becker, K.A. Reed, A. Voigt, and B. Medeiros, 2016: Thermodynamic control of anvil cloud amount. *Proc. Nat. Acad. Sci.*, **113**, 8927-8932.

Bouniol, D., R. Roca, T. Fiolleau, and D. E. Poan, 2016: Macrophysical, Microphysical, and Radiative Properties of Tropical Mesoscale Convective Systems over Their Life Cycle. *J. Clim.*, **29**, 3353–3371.

Chahine, M. T., et al., 2006: AIRS: Improving weather forecasting and providing new data on greenhouse gases. *Bull. Amer. Meteor. Soc.*, **87**, 911–926.

Duncan, D.I., C.D. Kummerow, and G.S. Elsaesser, 2014: A Lagrangian analysis of deep convective systems and their local environmental effects. *J. Clim.*, **27**, 2072-2086.

Duncan, D.I., and P. Eriksson, 2018: An update on global atmospheric ice estimates from satellite observations and reanalyses. *Atmos. Chem. Phys.*, **18**, 11205-11219.

Elsaesser, G.S., C.D. Kummerow, T.S. L'Ecuyer, Y.N. Takayabu, and S. Shige, 2010: Observed self-similarity of precipitation regimes over the tropical oceans. *J. Clim.*, **23**, 2686-2698.

Elsaesser, G.S., and C.D. Kummerow, 2013: A multisensor observational depiction of the transition from light to heavy rainfall on subdaily time scales. *J. Atmos. Sci.*, **70**, 2309-2324.

Elsaesser, G.S., A.D. Del Genio, J. Jiang, and M. van Lier-Walqui, 2017: An improved convective ice parameterization for the NASA GISS Global Climate Model and impacts on cloud ice simulation. *J. Clim.*, **30**, 317-336.

Feng, Z., X. Dong, B. Xi, S. A. McFarlane, A. Kennedy, B. Lin, and P. Minnis, 2012: Life cycle of midlatitude deep convective systems in a Lagrangian framework, *J. Geophys. Res.*, **117**, D23201, doi:10.1029/2012JD018362.

- 797 Feng, Z., L. R. Leung, R. A. Houze, S. Hagos, J. Hardin, Q. Yang, Q., et al., 2018: Structure and
798 evolution of mesoscale convective systems: Sensitivity to cloud microphysics in
799 convection-permitting simulations over the United States. *JAMES*, **10**, 1470–1494.
- 800 Feng, Z., R. A. Houze, L. R. Leung, F. Song, J. C. Hardin, J. Wang, W. I. Gustafson, and C. R.
801 Homeyer, 2019: Spatiotemporal Characteristics and Large-Scale Environments of
802 Mesoscale Convective Systems East of the Rocky Mountains. *J. Clim.*, **32**, 7303–7328.
- 803 Feng, Z., F. Song, K. Sakaguchi, and L. R. Leung, 2021: Evaluation of Mesoscale Convective
804 Systems in Climate Simulations: Methodological Development and Results from MPAS-
805 CAM over the United States. *J. Clim.*, **34**, 2611–2633.
- 806 Fiolleau, T., and R. Roca, 2013a: An algorithm for the detection and tracking of tropical mesoscale
807 convective systems using infrared images from geostationary satellite. *IEEE Trans.*
808 *Geosci. Remote Sens.*, **51**, 4302-4315.
- 809 Fiolleau, T., and R. Roca, 2013b: Composite life cycle of tropical mesoscale convective systems
810 from geostationary and low Earth orbit satellite observations: method and sampling
811 considerations. *Q. J. R. Meteorol. Soc.*, **139**, 941-953.
- 812 Fiolleau, T., R. Roca, S. Cloché, D. Bouniol, P. Raberanto, 2020: Homogenization of geostationary
813 infrared imager channels for cold cloud studies using Megha-Tropiques/ScaRaB. *IEEE*
814 *Trans. Geosci. Remote Sens.*, **58**, 6609-6622.
- 815 Futyán, J., and A. D. Del Genio, 2007: Deep convective system evolution over Africa and the
816 tropical Atlantic. *J. Clim.*, **20**, 5041-5060.
- 817 Gasparini B., P. N. Blossey, D. L. Hartmann, G. Lin, and J. Fan, 2019: What drives the life cycle
818 of tropical anvil clouds? *JAMES*, **11**, 2586–2605. <https://doi.org/10.1029/2019MS001736>.
- 819 Giangrande, S. E., T. Toto, M. P. Jensen, M. J. Bartholomew, Z. Feng, A. Protat, C. R. Williams,
820 C. Schumacher, and L. Machado, 2016: Convective cloud vertical velocity and mass-flux
821 characteristics from radar wind profiler observations during GoAmazon2014/5. *J.*
822 *Geophys. Res. Atmos.*, **121**, 12891–12913.
- 823 Grecu, M., W.S. Olson, S.J. Munchak, S. Ringerud, L.Liao, Z.S. Haddad, B.L. Kelley, and S.F.
824 McLaughlin, 2016: The GPM combined algorithm. *J. Atmos. Ocean. Tech.*, **33**, 2225-2245.

- 825 Hagos, S., Z. Feng, S. McFarlane, and L. R. Leung, 2013: Environment and the Lifetime of
826 Tropical Deep Convection in a Cloud-Permitting Regional Model Simulation. *J. Atmos.*
827 *Sci.*, **70**, 2409–2425.
- 828 Hagos, S., Z. Feng, R. S. Plant, and A. Protat, 2020: A machine learning assisted development of
829 a model for the populations of convective and stratiform clouds. *JAMES*, **12**, doi:
830 10.1029/2019MS001798.
- 831 Hannah, W.M., B.E. Mapes, and G.S. Elsaesser, 2016: A Lagrangian view of moisture dynamics
832 during DYNAMO. *J. Atmos. Sci.*, **73**, 1967-1985.
- 833 Hartmann, D.L., H.H. Hendon, and R.A. Houze Jr., 1984: Some implications of the mesoscale
834 circulations in tropical cloud clusters for large-scale dynamics and climate. *J. Atmos. Sci.*,
835 **41**, 113-121.
- 836 Hartmann, D.L., and K. Larson, 2002: An important constraint on tropical cloud-climate feedback.
837 *Geophys. Res. Letters*, **29**, 1951, doi:10.1029/2002GL015835.
- 838 Holloway, C.E., A.A. Wing, S. Bony, C. Muller, H. Masunaga, T.S. L'Ecuyer, D.D. Turner, and
839 P. Zuidema, 2017: Observing convective aggregation. *Surv. Geophys.*, **38**, 1199-1236.
- 840 Houze, R. A. Jr., 1989: Observed structure of mesoscale convective systems and implications for
841 large scale heating. *Quart. J. R. Meteor. Soc.*, **115**, 425– 461.
- 842 Houze, R. A. Jr., 1997: Stratiform Precipitation in Regions of Convection: A Meteorological
843 Paradox? *Bull. Amer. Meteor. Soc.*, **78**, 2179–2196.
- 844 Houze, R. A., 2004: Mesoscale convective systems. *Rev. Geophys.* **42**, 1–43.
- 845 Iguchi, T., S. Seto, et al., 2012: An overview of the precipitation retrieval algorithm for the Dual-
846 frequency Precipitation Radar (DPR) on the Global Precipitation Measurement (GPM)
847 mission's core satellite. <https://doi.org/10.1117/12.976823>.
- 848 Inoue, K., and L. Back, 2015: Column-Integrated Moist Static Energy Budget Analysis on Various
849 Time Scales during TOGA COARE, *J. Atmos. Sci.*, **72**, 1856-1871.
- 850 Khouider, B., J. Biello, and A. J. Majda, 2010: A Stochastic Multicloud Model for Tropical
851 Convection. *Commun. Math. Sci.*, **8**, 187–216.
- 852 Kiladis, G. N., K. H. Straub, and P. T. Haertel, 2005: Zonal and vertical structure of the Madden–

- 853 Julian oscillation. *J. Atmos. Sci.*, **62**, 2790–2809.
- 854 Knapp, K. R., M. C. Kruk, D. H. Levinson, H. J. Diamond, and C. J. Neumann, 2010: The
855 International Best Track Archive for Climate Stewardship (IBTrACS), *Bull. Amer. Meteor.*
856 *Soc.*, **91**(3), 363-376.
- 857 Kumar, V. V., C. Jakob, A. Protat, C. R. Williams, and P. T. May, 2015: Mass-Flux Characteristics
858 of Tropical Cumulus Clouds from Wind Profiler Observations at Darwin, Australia. *J.*
859 *Atmos. Sci.*, **72**, 1837–1855.
- 860 Lang, S.E., and W.-K. Tao, 2018: The next-generation Goddard Convective-Stratiform Heating
861 algorithm: New tropical and warm season retrievals for GPM. *J. Clim.*, **31**, 5997-6026.
- 862 Lin, J., B. E. Mapes, M. Zhang, and M. Newman, 2004: Stratiform precipitation, vertical heating
863 profiles, and the Madden–Julian oscillation. *J. Atmos. Sci.*, **61**, 296–309.
- 864 Lin, L., Q. Fu, X. Liu, Y. Shan, S.E. Giangrande, G.S. Elsaesser, K. Yang, and D. Wang,
865 2021: Improved convective ice microphysics parameterization in the NCAR CAM
866 model. *J. Geophys. Res. Atmos.*, **126**, no. 9, e2020JD034157, doi:10.1029/2020JD034157.
- 867 Liu, C., E. J. Zipser, D. J. Cecil, S. W. Nesbitt, and S. Sherwood, 2008: A Cloud and Precipitation
868 Feature Database from Nine Years of TRMM Observations. *J. Appl. Meteor. Clim.*, **47**,
869 2712-2728.
- 870 Liu, C., 2011: Rainfall Contributions from Precipitation Systems with Different Sizes, Convective
871 Intensities, and Durations over the Tropics and Subtropics, *J. Hydrometeor.*, **12**, 394-412.
- 872 Liu, C., S. Shige, Y. N. Takayabu, and E. Zipser, 2015: Latent Heating Contribution from
873 Precipitation Systems with Different Sizes, Depths, and Intensities in the Tropics, *J. Clim.*,
874 **28**, 186-203.
- 875 Lucas, C., E. J. Zipser, and M. A. Lemone, 1994: Vertical velocity in oceanic convection off
876 tropical Australia. *J. Atmos. Sci.*, **51**(21), 3183-3193.
- 877 Machado, L.A.T., W.B. Rossow, R.L. Guedes, and A.W. Walker, 1998: Life cycle variations of
878 mesoscale convective systems over the Americas. *Mon. Wea. Rev.*, **126**, 1630-1654.
- 879 Machado, L.A.T, and H. Laurent, 2004: The convective system area expansion over Amazonia
880 and its relationship with convective system life duration and high-level wind divergence.

- 881 *Mon. Wea. Rev.*, **132**, 714–725.
- 882 Mapes, B., and R. Neale, 2011: Parameterizing convective organization to escape the entrainment
883 dilemma. *JAMES*, **3**, M06004, doi:10.1029/2011MS000042.
- 884 Mauritsen, T., and Coauthors, 2012: Tuning the climate of a global model. *J. Adv. Model. Earth*
885 *Syst.*, **4**, M00A01, doi:10.1029/2012MS000154.
- 886 Moncrieff, M.W., C. Liu, and P. Bogenschutz, 2017: Simulation, modeling, and dynamically based
887 parameterization of organized tropical convection for global climate models. *J. Atmos.*
888 *Sci.*, **74**, 1363-1380.
- 889 Moncrieff, M. W., 2019: Toward a Dynamical Foundation for Organized Convection
890 Parameterization in GCMs. *Geophys. Res. Lett.*, **46**, 14103– 14108.
- 891 Naud, C.M., A.D. Del Genio, M. Bauer, and W. Kovari, 2010: Cloud vertical distribution across
892 warm and cold fronts in CloudSat-CALIPSO data and a general circulation model. *J.*
893 *Clim.*, **23**, 3397-3415.
- 894 Naud, C. M., J. F. Booth, J. F., and A. D. Del Genio, 2016: The Relationship between Boundary
895 Layer Stability and Cloud Cover in the Post-Cold-Frontal Region, *J. Clim.*, **29**, 8129-8149.
- 896 Nesbitt, S. W., R. Cifelli, and S. A. Rutledge, 2006: Storm Morphology and Rainfall
897 Characteristics of TRMM Precipitation Features. *Mon. Weather Rev.*, **134**, 2702–2721.
- 898 Parker, M. D., and R. H. Johnson, 2000: Organizational Modes of Midlatitude Mesoscale
899 Convective Systems. *Mon. Wea. Rev.*, **128**, 3413–3436.
- 900 Prein, A. F., C. Liu, K. Ikeda, S. B. Tier, R. M. Rasmussen,, G. J. Holland, and M. P. Clark, 2017:
901 Increased rainfall volume from future convective storms in the US. *Nat. Clim. Chang.*, **7**,
902 880–884.
- 903 Rapp, A.D., G. Elsaesser, and C. Kummerow, 2009: A combined multisensor optimal estimation
904 retrieval algorithm for oceanic warm rain clouds. *J. Appl. Meteorol. Climatol.*, **48**, 2242-
905 2256.
- 906 Retsch, M. H., C. Jakob, and M. S. Singh, 2020: Assessing Convective Organization in Tropical
907 Radar Observations. *J. Geophys. Res.: Atmos.*, **125**, e2019D031801.
- 908 Roca, R., J. Aublanc, P. Chambon, T. Fiolleau, and N. Viltard, 2014: Robust Observational

- 909 Quantification of the Contribution of Mesoscale Convective Systems to Rainfall in the
910 Tropics. *J. Clim.*, **27**, 4952–4958.
- 911 Roca, R., T. Fiolleau, and D. Bouniol, 2017: A simple model of the life cycle of mesoscale
912 convective system cloud shield in the tropics. *J. Clim.*, **30**, 4283-4298.
- 913 Roca, R., and T. Fiolleau, 2020: Extreme precipitation in the tropics is closely associated with
914 long-lived convective systems. *Commun. Earth. Environ.* **1**, 18.
915 <https://doi.org/10.1038/s43247-020-00015-4>.
- 916 Schiro, K. A., S. C. Sullivan, Y.-H. Kuo, H. Su, P. Gentine, G. S. Elsaesser, J. H. Jiang, J. D.
917 Neelin, 2020: Environmental controls on tropical mesoscale convective system
918 precipitation intensity. *J. Atmos. Sci.*, **77**, 4233-4249.
- 919 Schmidt, G.A., D. Bader, L.J. Donner, G.S. Elsaesser, J.-C. Golaz, C. Hannay, A. Molod, R. Neale,
920 and S. Saha, 2017: Practice and philosophy of climate model tuning across six U.S.
921 modeling centers. *Geosci. Model Dev.*, **10**, 3207-3223, doi:10.5194/gmd-10-3207-2017.
- 922 Schneider, T., S. Lan, A. Stewart, and J. Teixeira, 2017: Earth system modeling 2.0: A blueprint
923 for models that learn from observations and targeted high-resolution simulations. *Geophys.*
924 *Res. Lett.*, **44**, 12396-12417.
- 925 Schumacher, C. and R. A. Houze Jr., 2003a: Stratiform rain in the tropics as seen by the TRMM
926 Precipitation Radar. *J. Clim.*, **116**, 1739-1756.
- 927 Schumacher, C. and R. A. Houze Jr., 2003b: The TRMM Precipitation Radar’s view of shallow,
928 isolated rain. *J. Appl. Meteorol.*, **42**, 1519-1524.
- 929 Schumacher, C., R.A. Houze Jr., and I. Kraucunas, 2004: The tropical dynamical response to latent
930 heating estimates derived from the TRMM Precipitation Radar. *J. Atmos. Sci.*, **61**, 1341-
931 1358.
- 932 Schumacher, C. and R. A. Houze Jr., 2006: Stratiform precipitation production over sub-Saharan
933 Africa and the tropical East Atlantic as observed by TRMM. *Q.J.R. Meteorol. Soc.*, **132**,
934 2235-2255.
- 935 Seeley, J. T., N. Jeevanjee, W. Langhans, and D. M. Romps, 2019: Formation of tropical anvil
936 clouds by slow evaporation. *Geophys. Res. Lett.*, **46**,

- 937 <https://doi.org/10.1029/2018GL080747>.
- 938 Sherwood, S. C., M. J. Webb, J. D. Annan, J. D., K. C. Armour, P. M. Forster, J. C. Hargreaves,
939 et al., 2020: An assessment of Earth's climate sensitivity using multiple lines of
940 evidence. *Reviews of Geophysics*, **58**, e2019RG000678.
- 941 Shige, S., Y.N. Takayabu, S. Kida, W.-K. Tao, X. Zeng, C. Yokoyama, and T. L'Ecuyer, 2009:
942 Spectral retrieval of latent heating profiles from TRMM PR data. Part IV: Comparisons of
943 lookup tables from two- and three-dimensional simulations. *J. Clim.*, **22**, 5577-5594.
- 944 Skofronick-Jackson, et al., 2017: The Global Precipitation Measurement (GPM) Mission for
945 Science and Society, *Bull. Amer. Meteor. Soc.*, **98**, 1679-1695.
- 946 Sobel, A. H., J. Nilsson, and L. M. Polvani, 2001: The Weak Temperature Gradient Approximation
947 and Balanced Tropical Moisture Waves, *J. Atmos. Sci.*, **58**, 3650-3665.
- 948 Takahashi, H., Z. J. Luo, and G. L. Stephens, 2017: Level of neutral buoyancy, deep convective
949 outflow, and convective core: New perspectives based on 5 years of CloudSat data. *J.*
950 *Geophys. Res.: Atmos.*, **122(5)**, 2958-2969.
- 951 Takahashi, H., Z. J. Luo, and G. L. Stephens, 2021: Revisiting the entrainment relationship of
952 convective plumes: A perspective from global observations, *Geophys. Res. Lett.*,
953 <https://doi.org/10.1029/2020GL092349>.
- 954 Tan, J., C. Jakob, W.B. Rossow, and G. Tselioudis, 2015: Increases in tropical rainfall driven by
955 changes in frequency of organized deep convection. *Nature*, **519**, 451-454.
- 956 Tao, W.-K., and M. W. Moncrieff, 2009: Multiscale cloud system modeling. *Rev. Geophys.*, **47**,
957 RG4002, doi:10.1029/2008RG000276.
- 958 Tao, W.-K., and Co-Authors, 2016: TRMM Latent Heating Retrieval: Applications and
959 Comparisons with Field Campaigns and Large-Scale Analyses. *Meteor. Monographs*, **56**,
960 2.1-2.34.
- 961 Tao, W.-K., T. Iguchi, and S. Lang, 2019: Expanding the Goddard CSH Algorithm for GPM: New
962 Extratropical Retrievals. *J. Appl. Meteor. Clim.*, **58**, 921-946.
- 963 Teixeira, J., 2001: Cloud Fraction and Relative Humidity in a Prognostic Cloud Fraction
964 Scheme. *Mon. Wea. Rev.*, **129**, 1750–1753.

- 965 Tiedtke, M., 1993: Representation of Clouds in Large-Scale Models. *Mon. Wea. Rev.*, **121**, 3040
966 - 3061.
- 967 Tobin, I., S. Bony, and R. Roca, 2012: Observational evidence for relationships between the degree
968 of aggregation of deep convection, water vapor, surface fluxes, and radiation. *J. Climate*,
969 **25**, 6885-6904.
- 970 Tobin, I., S. Bony, C.E. Holloway, J.Y. Grandpeix, G. Seze, D. Coppin, S.J. Woolnough, and R.
971 Roca, 2013: Does convective aggregation need to be represented in cumulus
972 parameterizations? *JAMES*, **5**, 692-703.
- 973 Vant-Hull, B., W. Rossow, and C. Pearl, 2016: Global comparisons of regional life cycle properties
974 and motion of multiday convective systems: tropical and midlatitude land and ocean. *J.*
975 *Clim.* **29**, 5837–5858.
- 976 Wang, D., S. E. Giangrande, K. Schiro, M. P. Jensen, and R. A. Houze, 2019: The
977 characteristics of tropical and midlatitude mesoscale convective systems as revealed by
978 radar wind profilers. *J. Geophys. Res. Atmos.*, **124**, 4601– 4619.
- 979 Wang, D., S. E. Giangrande, Z. Feng, J. C. Hardin, and A. F. Prein, 2020: Updraft and downdraft
980 core size and intensity as revealed by radar wind profilers: MCS observations and idealized
981 model comparisons. *J. Geophys. Res. Atmos.*, **125**,
982 <https://doi.org/10.1029/2019JD031774>.
- 983 Waters, J. W., et al., 2006: The Earth Observing System Microwave Limb Sounder (EOS MLS)
984 on the Aura Satellite. *IEEE Trans. Geosci. Rem. Sens.*, **44**, 1075-1092.
- 985 Yuter, S. E., and R. A. Houze Jr., 1995: Three-dimensional kinematic and microphysical evolution
986 of Florida cumulonimbus. Part III: Vertical mass transport, mass divergence, and synthesis.
987 *Mon. Wea. Rev.*, **123**, 1964-1983.
- 988 Yuter, S. E., and R. A. Houze Jr., 1998: The natural variability of precipitating clouds over the
989 western Pacific warm pool. *Q. J. R. Meteorol. Soc.*, **124**, 53-99.
- 990 Zelinka, M.D., and D.L. Hartmann, 2010: Why is longwave cloud feedback positive? *J. Geophys.*
991 *Res.*, **115**, D16117, doi:10.1029/2010JD013817.
- 992 Zelinka, M.D., and D.L. Hartmann, 2011: The observed sensitivity of high clouds to mean surface

993 temperature anomalies in the tropics. *J. Geophys. Res.*, **116**, D23103,
994 doi:10.1029/2011JD016549.

995 Zipser, E. J., and M. A. LeMone, 1980: Cumulonimbus vertical velocity events in GATE. Part II:
996 Synthesis and model core structure. *J. Atmos. Sci.*, **37(11)**, 2458-2469.

997

998

999

1000

1001

1002

1003

1004

1005

1006

1007

1008

1009

1010

1011

1012

1013

1014

1015

1016

1017